https://doi.org/10.5194/egusphere-2026-1585
Preprint. Discussion started: 4 May 2026

Future learning and uncertainty reductions in projections of the Amery Ice Shelf catchment, Antarctica

Zach Zerbe[1], Sanket Jantre[2], Nathan M. Urban[2], Matthew J. Hoffman[3], and Trevor Hillebrand[3]

[1]Mathematics and Computer Science Department, Colorado College, Colorado Springs, CO, USA
[2]Applied Mathematics Department, Brookhaven National Laboratory, Upton, NY, USA
[3]Fluid Dynamics and Solid Mechanics Group, Los Alamos National Laboratory, Los Alamos, NM, USA

Correspondence: Sanket Jantre (sjantre@bnl.gov)

Abstract.

Antarctica's Lambert–Amery system is often considered resilient to future climate changes owing to strong buttressing by the Amery Ice Shelf, yet emerging projections through 2300 suggest that sustained ocean warming could substantially alter its long-term mass balance. While recent probabilistic studies quantify present-day parametric uncertainty and propagate it to future sea-level contribution projections, they do not assess how rapidly these uncertainties will contract as forthcoming observations are assimilated. Here we quantify future learning rates for the Amery sector by building a sequential Bayesian calibration workflow that uses present-day (year 2015) as well as synthetic future observations to evaluate how quickly forthcoming data can tighten projections of sea-level contribution through 2300. Using simulations from the MPAS-Albany Land Ice (MALI) model augmented by Gaussian process emulators, we first generate 100 synthetic future observation trajectories of cumulative grounded mass change at 15-year intervals (2030–2300) under a high-greenhouse-gas-emission scenario, drawing from the present-day posterior distributions of six uncertain input parameters related to ice flow, calving, and ice-shelf melting. For each trajectory, we then sequentially recalibrate parameters at each analysis year using the present-day and all synthetic observations available up to that year, and propagate the recalibrated parameter uncertainties to generate updated projections of sea-level contribution. We quantify learning as the reduction in 90% credible interval widths for both MALI parameters and sea-level contribution projections, characterizing variability across the 100 trajectories to assess uncertainty in the learning rate itself. Results reveal substantial but parameter-dependent learning, with the ice-shelf melt coefficient and basal slip exponent exhibiting the largest uncertainty reduction ($\gtrsim$ 8-fold by 2300). Learning about future sea-level contribution is time-horizon dependent: end-of-century (2100) projections show limited contraction (30% reduction in *very-likely* ranges), whereas year-2200 and year-2300 projections exhibit rapid learning ($\sim$ 6-fold reduction) after substantial ice-shelf thinning projected around 2150 creates stronger dynamic response which aids parameter learning. These findings indicate that near-term Amery contributions will remain difficult to tightly bound until substantial dynamical changes manifest (post-2150 in these simulations), but that sustained observations through that transition have high impact for reducing long-horizon risk. While our perfect-model assumption and simplified likelihood structure represent simplifications, the results provide guidance for assessing future learning of ice-sheet behavior.

https://doi.org/10.5194/egusphere-2026-1585
Preprint. Discussion started: 4 May 2026

1 Introduction

The mass change of the Antarctic Ice Sheet is one of the largest uncertainties in future sea-level change (Edwards et al., 2021; Fox-Kemper et al., 2021), creating deep uncertainty in coastal risk assessment and adaptation planning (Bakker et al., 2017-02; Kopp et al., 2019). The response of the Antarctic Ice Sheet to changes in climate is subject to threshold processes and instabilities related to ice flow and fracture, basal processes, and interactions with the atmosphere and ocean (Hanna et al., 2024; Noble et al., 2020; Pattyn and Morlighem, 2020). Ice-sheet models represent many of these processes with parameterizations that include uncertain parameters that can only be partially calibrated from historical observations, and sometimes not at all.

Because these uncertain processes propagate into sea-level projections, recent work has increasingly emphasized probabilistic frameworks, Bayesian calibration, and surrogate modeling to quantify parametric uncertainty and project it forward (Little et al., 2013; Lee et al., 2020; Wernecke et al., 2020; Bulthuis et al., 2019; Berdahl et al., 2021, 2023; Recinos et al., 2023). Methodologically, Bayesian calibration builds on foundational frameworks for calibrating models to uncertain observations while representing residual discrepancy (Kennedy and O'Hagan, 2001; Higdon et al., 2008). In ice-sheet contexts, these approaches are often coupled with computational strategies including statistical emulation, multi-fidelity methods, and reduced-order representations to make calibration and uncertainty propagation feasible for expensive transient simulations (e.g. Wernecke et al., 2020; Berdahl et al., 2021; Jakeman et al., 2025). Recent calibrated projections demonstrate the practical value of these ideas for constraining future ice-mass loss using present-day observations, particularly in dynamically sensitive regions (Bevan et al., 2023; Felikson et al., 2023; Aschwanden and Brinkerhoff, 2022; Coulon et al., 2024; Rosier et al., 2025).

However, even when present-day uncertainties are quantified, a critical gap remains: decision-makers need to understand not only today's uncertainty, but also the *rate at which uncertainty may shrink* as new observations accumulate. This "future learning" perspective is central to adaptive policy under deep uncertainty: if learning is expected to be rapid, it may support some degree of wait-and-see flexibility; if learning is slow, it strengthens the case for earlier precautionary action (Urban et al., 2014; Kelly and Kolstad, 1999; Leach, 2007; Hope, 2015). While learning-rate concepts have been explored extensively for climate sensitivity and related quantities (Urban et al., 2014; Leach, 2007; Libardoni et al., 2018), they have received substantially little attention for ice-sheet projections, which have unique challenges related to both susceptibility to abrupt instabilities and long response times.

Here, we explore the application of future learning methods to ice-sheet projections by focusing on a single drainage basin of the Antarctic Ice Sheet to aid interpretability. The Lambert–Amery system (hereafter "the Amery sector") drains a large fraction (16%) of the East Antarctic Ice Sheet (Fricker et al., 2002) and is a good target for exploring future learning because it has exhibited little historical change (King et al., 2009; Jantre et al., 2024), limiting the observed behavior over which parameters can be calibrated. Additionally, while the Amery sector has traditionally been considered comparatively resilient to ocean-driven changes because the Amery Ice Shelf provides strong buttressing (Pittard et al., 2017), recent work has suggested that sustained ocean warming could cause loss of the ice shelf and rapid increase in discharge of grounded ice into the ocean (Seroussi et al., 2024; Jantre et al., 2024). Thus, the Amery sector represents a situation where historical observations have a limited ability to constrain future behavior and there is a high potential for future learning.

https://doi.org/10.5194/egusphere-2026-1585
Preprint. Discussion started: 4 May 2026

To this end, we quantify future learning rates for the Amery sector by combining sequential Bayesian calibration with synthetic future observations of cumulative grounded mass change. We build directly on recent probabilistic projections for the Amery sector under high basal melt conditions (Jantre et al., 2024) to provide synthetic future observations. Our workflow explicitly represents uncertainty in key parameters controlling ice dynamics and ice-shelf melt forcing and evaluates how posterior predictive uncertainty in sea-level contribution evolves as additional synthetic future observations are assimilated. By doing so, we provide a quantitative characterization of learning timescales for a major Antarctic Ice Sheet sector and identify relationships between observational frequency/type and uncertainty reduction.

The remainder of the paper is organized as follows. Section 2 outlines the modeling approach, including the generation of synthetic future observations (Section 2.1), the sequential Bayesian calibration (Section 2.2), and the propagation of recalibrated uncertainties to probabilistic sea-level contribution projections (Section 2.3). Section 3 presents results on future learning of MALI parameters (Section 3.1) and learning of sea-level contribution projections across time horizons (Section 3.2). Section 4 interprets these findings, highlights implications for observing-system design and methodological choices, and places the work in the context of related studies. Section 5 offers concluding remarks and directions for future work.

2 Data and methods

We perform sequential Bayesian calibration of the model parameters for the Amery Ice Shelf (AmIS) catchment region using the MPAS-Albany Land Ice (MALI) (Hoffman et al., 2018) model-based perturbed-parameter simulation ensemble developed in Jantre et al. (2024). Specifically, we adopt the six MALI input parameters — ice stiffness scaling factor (C_ϕ), basal friction scaling factor (C_μ), basal slip exponent (q), calving yield stress (σ_{max}), ice-shelf melt coefficient (γ_0), and ice-shelf basal melt rate $(\overline{m})$ — and their expert-knowledge-driven priors from their work (refer to Table 1 of Jantre et al. (2024)). Following Kennedy and O'Hagan (2001), we update the parameter distributions conditioned on observations using Bayes' rule,

$$p(\theta|\mathcal{D}) \propto p(\mathcal{D}|\theta)p(\theta),$$

as additional data are considered sequentially. Accordingly, from Jantre et al. (2024) we also acquire the three observables — mass balance, grounding line movement, and calving front movement — for present-day (year 2015) calibration with corresponding Gaussian process (GP) emulators trained on the historical relaxation (RELX) ensemble. Furthermore, we adopt their SSP5 projection ensemble branched from RELX under UKESM SSP5-8.5 forcing ("expAE05" in Seroussi et al. (2024)) along with a Principal Component Analysis (PCA) GP emulator trained on this ensemble to generate time series projections of sea-level contribution from AmIS. We then adapt the future-learning framework of Urban et al. (2014) to quantify the rate at which additional observations over time in the future could tighten parameter posteriors and the associated sea-level contribution projections. Specifically, we define the *rate of learning*, or learning rate, as the reduction in the width of the 90% central credible intervals (IPCC "*very-likely*" range Kause et al. (2022)) of model parameters and sea-level contribution projections over time. Hereafter, all credible intervals reported are central credible intervals.

https://doi.org/10.5194/egusphere-2026-1585
Preprint. Discussion started: 4 May 2026

2.1 Synthetic future observations

We quantify the rate of future learning with additional synthetic observations of a single observational constraint: the *cumulative grounded mass change* of the AmIS catchment. For the present-day, we calibrate inputs using the three large-scale observables from Jantre et al. (2024) — mass balance (i.e., grounded mass-change rate), grounding-line, and calving-front movements — with their stated likelihood models. For $t > 2015$, we restrict attention to cumulative grounded mass change for two reasons. First, the rate variables used for present-day calibration fluctuate frequently, while cumulative changes integrate over them, naturally smoothing instantaneous changes — making cumulative measure a more stable target for statistical emulation than instantaneous rates. Second, for simplicity, we consider only one observable in the sequential Bayesian calibration for future years. As cumulative grounded mass change is the time integral of annual grounded mass-change rates, we propagate observational uncertainty by summation. To this end, the observational noise standard deviation of grounded mass change rate in 2015 is $5.720\ \mathrm{Gt\,yr^{-1}}$ (Jantre et al., 2024), and we assume this annual noise level persists unchanged through 2300. Then the observational noise variance for cumulative grounded mass change from year $t > 2016$ is given by

$$\sigma^2_{o,t} \;=\; (5.720\ \mathrm{Gt\,yr^{-1}})^2 \times \delta, \quad \text{with } \delta = t - 2016.$$

Hence, $\sigma^2_{o,t}$ grows linearly with δ, reflecting increasing observational uncertainty over time.

To generate synthetic future observations for sequential calibration, we proceed as follows. We obtain the simulated cumulative grounded mass change values from the SSP5 ensemble of Jantre et al. (2024). We then train scalar GP emulators that map the six input parameters to cumulative grounded mass change at every fifteenth year from 2030 to 2300, yielding 19 emulators. The GP emulators use a linear mean and a separable twice mean-square differentiable Matérn covariance kernel with smoothness parameter ($\nu = 2.5$), providing adequate smoothness while avoiding the over-smoothing associated with the infinitely differentiable squared-exponential kernel. Emulator skill is assessed via five-fold cross-validation (as in Jantre et al. (2024)); after validation, the emulators are refit on the full SSP5 ensemble for subsequent use. Cross-validation diagnostics for GP emulators of cumulative grounded mass change at years 2150 and 2300, as well as diagnostics assessing emulation skill jointly across all analysis years, are included in Appendix A. We omit these diagnostics for the remaining individual analysis years for brevity.

Next, we draw 100 input-parameter vectors, θ_i, from the present-day posterior and pass them through the 19 GP emulators for the selected analysis years, producing 100 estimates of cumulative grounded mass change for each analysis year $t \in \{2030, 2045, \ldots, 2300\}$. We then form each synthetic future observation of cumulative grounded mass change by sampling from $N(\mu_{t,i},\ \sigma^2_{o,t} + \sigma^2_{c,t,i})$, where $\mu_{t,i}$ is the emulator prediction at the t-th analysis year for the i-th parameter vector draw (θ_i). Furthermore, $\sigma^2_{c,t,i}$ denotes the code uncertainty which is the GP predictive variance at (θ_i, t), capturing the emulator error. We treat this term as independent of the observational variance $\sigma^2_{o,t}$ and set the sampling variance to $\sigma^2_{o,t} + \sigma^2_{c,t,i}$ when generating synthetic observations. Fig. 1 illustrates a few synthetic future observation trajectories. These synthetic observation trajectories are then used in our sequential Bayesian calibration to update parameter posteriors year by year and to quantify the rate of future learning. In other words, each of these synthetic future observation time-series represents a possible future trajectory of

https://doi.org/10.5194/egusphere-2026-1585
Preprint. Discussion started: 4 May 2026

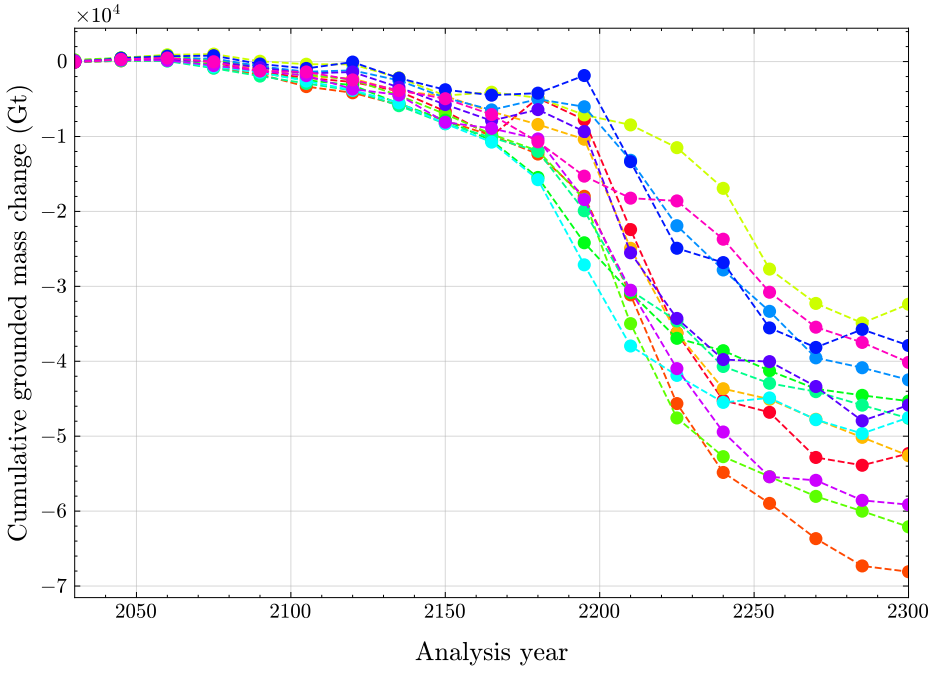

Figure 1. Example synthetic future-observation trajectories of cumulative grounded mass change, sampled every 15 years from 2030 to 2300

the AmIS catchment's cumulative grounded mass change; because we cannot know the true future trajectory, we consider the 100 sampled future trajectories based on the Bayesian calibration of model parameters to the present-day observables.

2.2 Sequential Bayesian calibration

We perform sequential Bayesian calibration using the synthetic future observations described above. For each analysis year $t \in \mathcal{T} = \{2030, 2045, \cdots, 2300\}$, the observable data comprise (i) three present-day observables and (ii) the cumulative grounded mass change evaluated at all quindecennial (15-year) times $t' \in \mathcal{T}$ with $t' \leq t$. We map the MALI inputs to each observable using their corresponding scalar GP emulators — three GPs for the present-day observables and one scalar GP each for the cumulative grounded mass change for all the years evaluated up to and including the analysis year t.

Starting from the posterior conditioned on the 2015 observables ("present-day posterior"), we update the parameter posteriors separately for each analysis year t using all the observables up to t. The likelihood is modeled as a product of univariate Gaussian distributions across observables, i.e., a multivariate Gaussian with diagonal covariance. For the 2015 metrics, likelihood variances add observational and code uncertainties (as in Jantre et al. (2024)). For cumulative grounded mass change at analysis year t and current parameter vector draw θ_i, we use $\sigma^2_{o,t}$ from the previous section and add code uncertainty $\sigma^2_{c,t,i}$, so the effective variance is $\sigma^2_{o,t} + \sigma^2_{c,t,i}$. For tractability, we assume independence among the 2015 observables (as in Jantre et al. (2024)) and across future years for the cumulative grounded mass-change observations; we acknowledge that this may understate temporal correlation and treat it as a limitation. Bayesian calibration and sequential updating follow Kennedy and

https://doi.org/10.5194/egusphere-2026-1585
Preprint. Discussion started: 4 May 2026

O'Hagan (2001). Posterior sampling at each t uses the No-U-Turn Sampler (NUTS) with a dense covariance matrix, drawing 100,000 samples per calibration (after 100,000 burn-in samples), using the probabilistic programming language `Turing.jl` (Fjelde et al., 2025).

To quantify sensitivity to future observations considered, we treat each set of synthetic future observations over quindecennial times in $\{2030, 2045, \cdots, 2300\}$ collected by drawing a single input parameter vector from the present-day posterior as a distinct future trajectory with a sequence of observables: $\{y_{2030}, y_{2045}, \ldots, y_{2300}\}$. In turn, the calibrations are parallelized across the 100 trajectories, with each trajectory involving 19 analysis years, yielding 1900 concurrent calibration runs on a high-performance computing cluster.

2.3 Probabilistic future learning

We propagate uncertainties in MALI parameters through a multivariate PCA GP emulator, adopted from Jantre et al. (2024), trained and validated on a low-dimensional representation of volume-above-flotation (VAF) change time series from the SSP5 projection ensemble. Emulator outputs are then converted to sea-level equivalent (SLE) following definitions in Goelzer et al. (2020), yielding probabilistic SLE projections. Specifically, the leading five principal components of the VAF-change time series are emulated using scalar GPs as functions of the MALI parameters. Emulator predictions in PC space are back-transformed to the full space to obtain distributions of future VAF-change, which are then converted to SLE projections.

To this end, for each of the 100 synthetic future observation trajectories of the AmIS catchment generated in Section 2.1, we repeat the sequential Bayesian calibration procedure described in Section 2.2 to obtain parameter posteriors at each analysis year $t \in \mathcal{T}$. We evaluate the probabilistic rate of future learning of model parameters via reductions in credible-interval widths across the 100 trajectories, thereby capturing the associated uncertainty. Next, we recalibrate our SLE projections by propagating the recalibrated posterior samples of model parameters through the PCA GP emulator, as if new observations became available every 15 years (Sec. 2.2) to quantify how uncertainty (measured by credible-interval width) in the future SLE projections contracts with additional "observed" information. We repeat this procedure across all 100 trajectories to characterize the range of future-learning behaviors, since the true trajectory of observations in the future is unknown and each synthetic trajectory yields a different future-learning behavior. This, in turn, allows us to quantify uncertainty in the rate of future learning of probabilistic projections of sea-level contribution.

3 Results

3.1 Probabilistic future learning of MALI parameters from sequential Bayesian calibration

Fig. 2 illustrates sequential Bayesian calibration by showing the posterior distributions of the MALI parameters for a single synthetic future-observation trajectory. As additional observations of cumulative grounded mass change are assimilated, parameter posterior distributions contract markedly. The posterior contractions are significant for all parameters, with especially large uncertainty reductions for the basal slip exponent (q), basal friction scaling factor (C_μ), and ice-shelf melt coefficient (γ_0). As

https://doi.org/10.5194/egusphere-2026-1585
Preprint. Discussion started: 4 May 2026

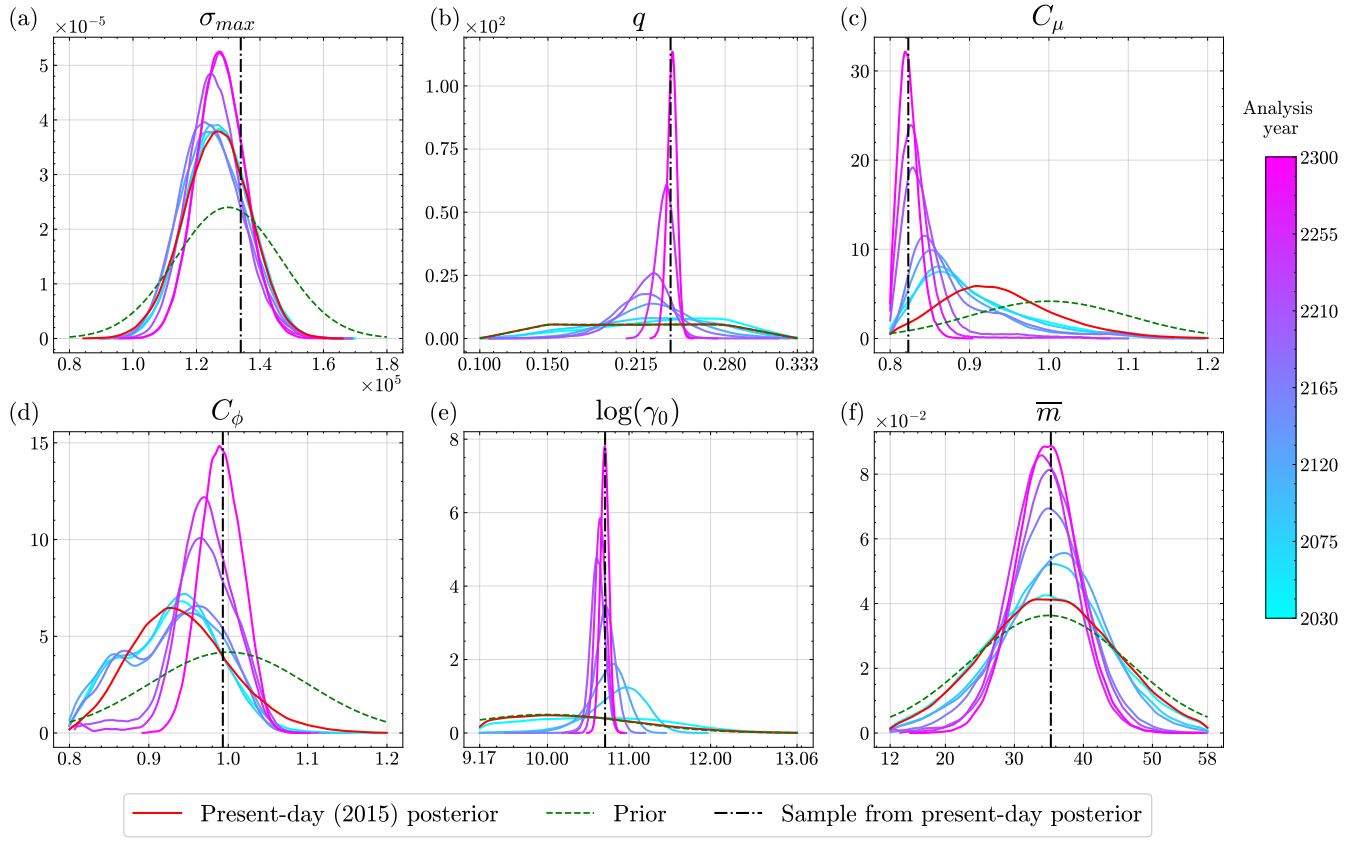

Figure 2. Sequential Bayesian calibration of MALI parameters, illustrated by their kernel density estimates across analysis years for a single randomly chosen future-observation trajectory. Present-day (year 2015) posteriors and priors are shown as red solid and green dashed lines, respectively. The sample from the present-day posterior used to generate the underlying synthetic future-observation trajectory is indicated by a vertical black dash-dotted line.

a further illustration, we extend this analysis in Fig. 3, which summarizes results for future learning of MALI parameters across four randomly selected future-observation trajectories (one of which matches Fig. 2 and is shown as the plum-colored trajectory with a corresponding similarly shaded, fainter confidence band). We observe substantial future learning for the basal and ice-shelf slip exponents as additional observations are incorporated into calibration. The remaining parameters show reduced uncertainties but remain indiscernible across trajectories due to significant overlap among their shaded credible interval bands by 2300. The apparently weaker learning for these other parameters largely reflects the summary chosen here — plotting 90% credible intervals around the posterior mean over analysis years — versus the full posterior densities in Fig. 2, where visual attention tends to focus on the peak. We also observe that the recalibrated posterior means generally converge to the parameter values used to generate the corresponding future-observation trajectories, with one exception of calving yield stress (σ_{max}). This misalignment in case of σ_{max} is possibly due to the finite time horizon considered in sequential Bayesian calibration and

https://doi.org/10.5194/egusphere-2026-1585
Preprint. Discussion started: 4 May 2026

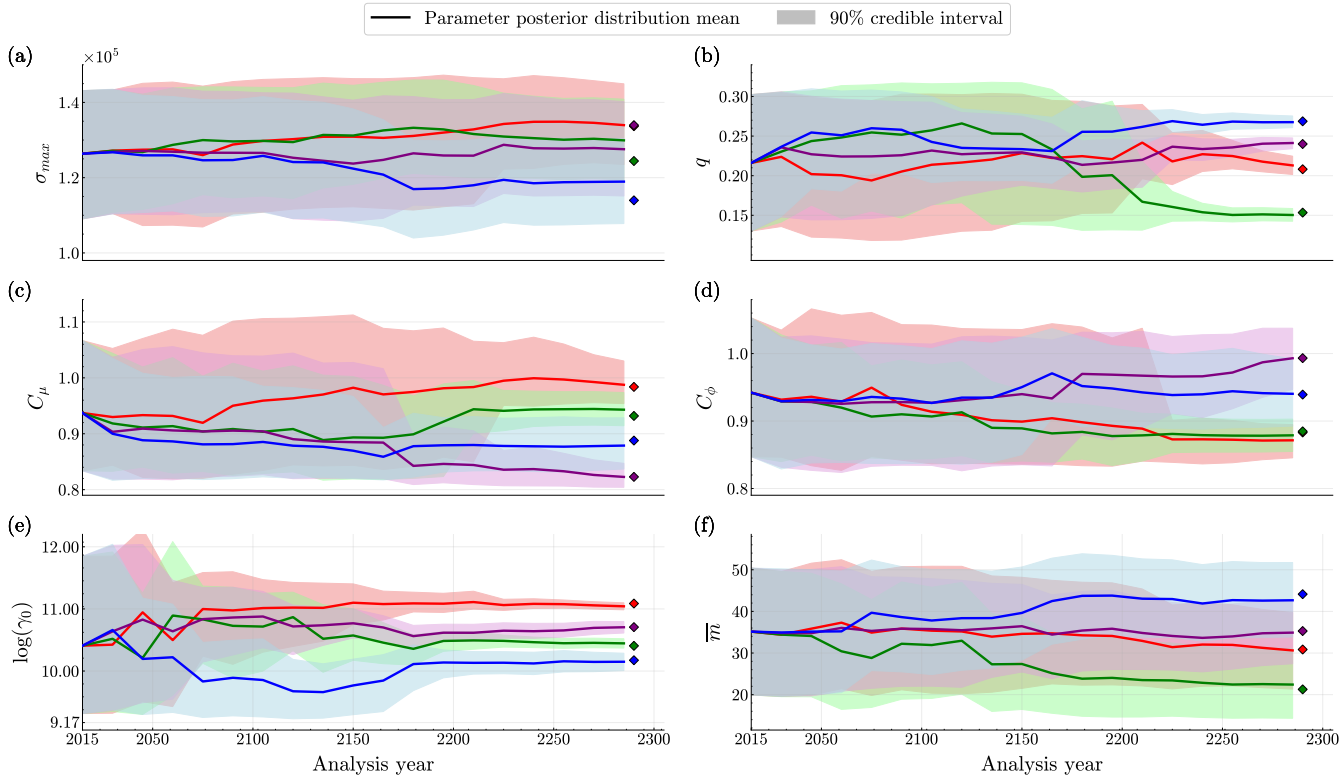

Figure 3. Future learning of MALI parameters over time for four randomly chosen synthetic future-observation trajectories. Thick lines and shaded bands denote posterior means (*best estimate*) and associated 90% credible intervals (*very-likely* range), respectively. Diamonds on the right of each panel indicate the parameter values drawn from its present-day (year 2015) posterior used to generate corresponding synthetic future-observation trajectory.

incorporating additional observables over the same period or extending the horizon beyond 2300 could ameliorate it, which we leave for future work.

Having demonstrated future learning for one and four trajectories as illustrations, we now turn to evaluating future learning for the entire ensemble of the 100 sampled trajectories. To assess reductions in parameter uncertainty across all trajectories, Fig. 4 summarizes, for each parameter across analysis years, the width of the 90% credible interval (*very-likely* range). Specifically, we plot the across-trajectory mean (*best estimate*) learning curve with 66% credible-interval bands indicating the *likely* ranges, per IPCC usage (Kause et al., 2022). This framing allows us to evaluate the probabilistic rate of future learning for the MALI parameters. To this end, uncertainty reduction occurs across all parameters, a result less apparent in Fig. 3 because of overlapping *very-likely* parameter ranges. By 2300, the across-trajectory *best estimate* of the *very-likely* range width is reduced substantially for $\log(\gamma_0)$ and q, and moderately for σ_{max}, C_μ, C_ϕ, and $\overline{m}$. Consistent with their discernible learning curves in Fig. 3, the largest uncertainty reductions are observed for ice-shelf melt coefficient and basal friction exponent: for $\log(\gamma_0)$, 2.532 in 2015 to 0.250 [0.136 to 0.386] in 2300; for q, 0.172 in 2015 to 0.021 [0.015 to 0.025] in 2300. These changes

https://doi.org/10.5194/egusphere-2026-1585
Preprint. Discussion started: 4 May 2026

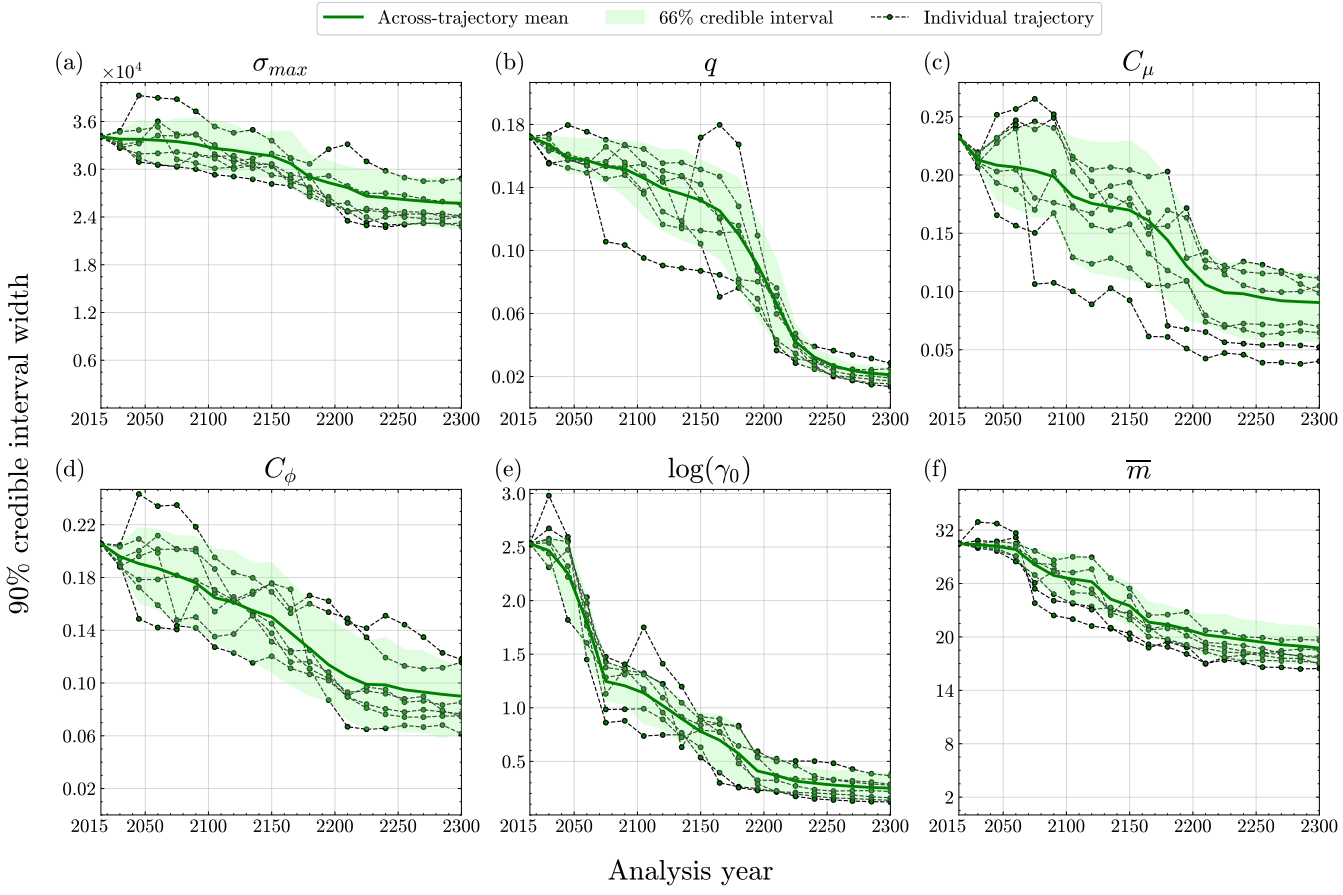

Figure 4. Future learning of MALI parameters. Evolution of parameter uncertainties over time across 100 synthetic future-observation trajectories generated and assimilated using sequential Bayesian calibration. We assess future learning using the width of the 90% credible intervals (*very-likely* ranges) for each parameter at each analysis year across future trajectories; smaller values indicate greater learning. Example trajectories of 90% credible interval widths over time are shown using dashed lines for a few individual future trajectories used for calibration, illustrating trajectory-to-trajectory variability in learning arising from different realizations of synthetic future observations. The thick curve is the across-trajectory mean (*best estimate*) of the *very-likely* range widths and the shaded band denotes the across-trajectory 66% credible interval (*likely* range), summarizing how quickly uncertainty is expected to contract on average and how uncertain that contraction is, respectively. By 2300, the uncertainties in MALI parameters are reduced substantially for $\log(\gamma_0)$ and q, and moderately for σ_{max}, C_μ, C_ϕ, and $\overline{m}$. We also provide same plot without the example trajectories of future learning in Fig. B1 of Appendix B.

correspond to an $\sim 10\times$ reduction in uncertainty for $\log(\gamma_0)$ and an $\sim 8\times$ reduction for q. For $\log(\gamma_0)$, reduction is fast until 2075, moderate from 2075–2195, and slower from 2195–2300, with the *likely* band remaining narrow until 2075, then widening slightly and staying roughly constant through 2300. For q, reduction is gradual through 2165, rapid from 2165–2225, and slower from 2225–2300, with the *likely* band widening gradually until 2180, after which narrowing through 2300.

https://doi.org/10.5194/egusphere-2026-1585
Preprint. Discussion started: 4 May 2026

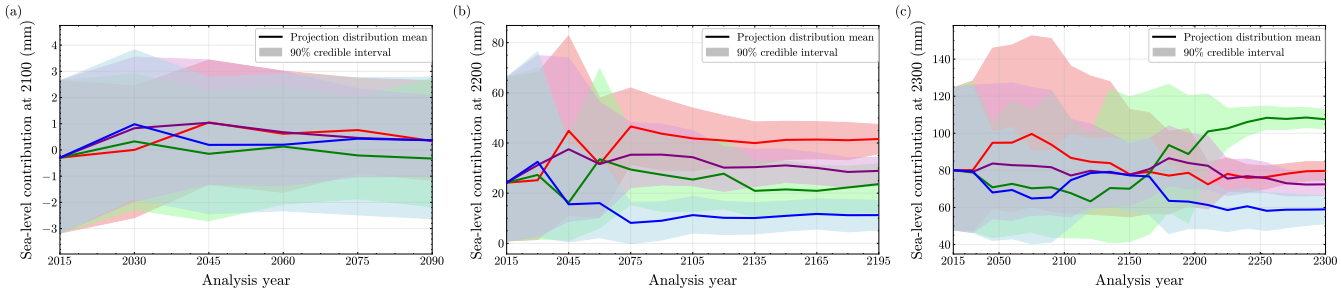

Figure 5. Future learning of sea-level contribution (millimeters SLE) projections at years (a) 2100, (b) 2200, and (c) 2300 across the same four future trajectories considered in Fig. 3. Thick lines denote posterior predictive means (*best estimate*) of SLE projections; shaded bands denote 90% credible intervals (*very-likely* ranges).

For σ_{max}, uncertainties reduce from 34.09 kPa in 2015 to 25.73 [22.53 to 28.80] kPa in 2300 — an $\sim 25\%$ reduction. The reductions are slow till 2150, moderate from 2150–2225, and again slow from 2225–2300, with *likely* band widening till 2045 and staying roughly constant through 2300. For C_μ, uncertainties reduce from 0.233 in 2015 to 0.091 [0.056 to 0.114] in 2300–an $\sim 60\%$ reduction. The reductions are moderate till 2150, faster from 2150–2225, and slower from 2225–2300, with *likely* band gradually widening till 2150, narrowing from 2150–2195, and then stay roughly constant through 2300. For C_ϕ, uncertainties reduce from 0.206 in 2015 to 0.090 [0.062 to 0.113] in 2300–an $\sim 56\%$ reduction. The reductions are moderate till 2150, slightly faster from 2150–2225, and slower from 2225–2300, with *likely* band widening till 2045 and staying roughly constant through 2300. For $\overline{m}$, uncertainties reduce from 30.48 Gt yr^{-1} in 2015 to 18.75 [16.83 to 20.99] Gt yr^{-1} in 2300–an $\sim 38\%$ reduction. The reductions are slow till 2060, faster from 2060–2165, and slower from 2165–2300, with *likely* band widening till 2120, slightly narrowing from 2120–2165, and then staying roughly similar through 2300.

3.2 Probabilistic future learning of sea-level contribution projections

In order to examine how sequentially calibrated MALI parameters would impact the SLE projections, we generate 5,000 samples of recalibrated MALI parameters over analysis years across the 100 future trajectories. We then propagate these samples through the PCA GP emulator trained on the SSP5 projection ensemble to predict SLE time series projections through 2300. For concision, we only report the future learning results for SLE projections at 2100, 2200, and 2300. Fig. 5 illustrates future learning of SLE projections at 2100, 2200, and 2300 across the same four future trajectories as in Fig. 3. Across those trajectories, SLE projection uncertainties at 2100 (Fig. 5a) remain indiscernible as information from more future years is introduced due to overlapping *very-likely* ranges. For SLE projections at 2200 (Fig. 5b) and 2300 (Fig. 5c), we observe substantial future learning across each trajectory over analysis years as additional observations are included in calibration.

We evaluate future learning of SLE projections across all 100 trajectories in Fig. 6 using the widths of the *very-likely* SLE ranges at 2100, 2200, and 2300. We plot the across-trajectory mean (*best estimate*) curve of those widths as well as their *likely* bands. For 2100 (Fig. 6a), uncertainty declines from 5.89 mm SLE in 2015 to 4.17 [2.80 to 5.09] mm SLE in 2090, a 30%

https://doi.org/10.5194/egusphere-2026-1585
Preprint. Discussion started: 4 May 2026

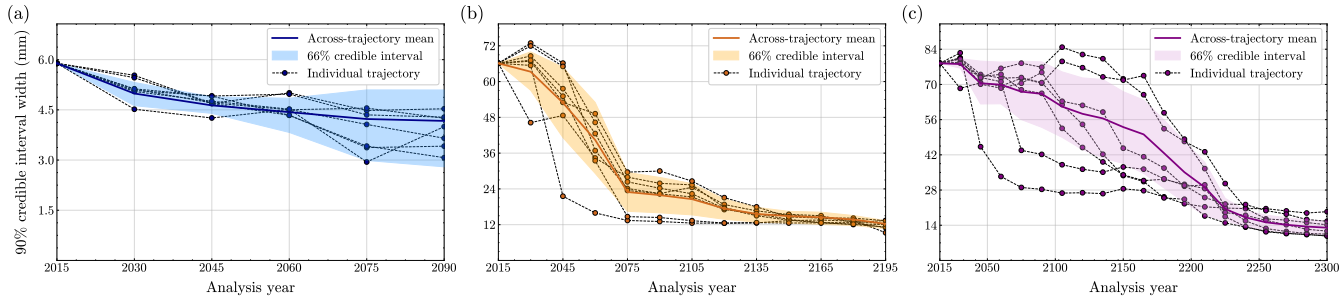

Figure 6. Future learning of sea-level contribution projections. Evolution of sea-level contribution (millimeters SLE) projection uncertainty at (a) 2100, (b) 2200, and (c) 2300 across 100 independent synthetic future–observation trajectories generated and assimilated using sequential Bayesian calibration. We assess future learning using the width of the 90% credible intervals (*very-likely* ranges) for each projection year's sea-level contribution at each analysis year across future trajectories; smaller values indicate greater learning. Example trajectories of 90% credible-interval widths over time are shown using dashed lines for a few individual future trajectories used for calibration, illustrating trajectory-to-trajectory variability in learning arising from different synthetic future-observation trajectories. The thick curve is the across-trajectory mean (*best estimate*) trajectory and the shaded band denotes the across-trajectory 66% credible interval (*likely* range), summarizing how quickly uncertainty is expected to contract on average and how uncertain that contraction is, respectively. We also provide same plot without the example trajectories of future learning in Fig. B2 of Appendix B.

reduction, with slow decline throughout the learning period and widening *likely* band. For 2200 (Fig. 6b), uncertainty reduces from 66.13 mm SLE in 2015 to 12.28 [10.65 to 13.37] mm SLE in 2195, an $\sim$ 6-fold reduction, with fast contraction until 2075 and gradual reduction from 2075–2195. Moreover, the *likely* band remains wide until 2105, after which it reduces gradually from 2105–2195. For 2300 (Fig. 6(c)), uncertainty reduces from 78.40 mm SLE in 2015 to 13.02 [10.24 to 15.47] mm SLE in 2300, an $\sim 6\times$ reduction, contracting at a moderate rate until 2225 and at slow rate thereafter from 2225–2300. Herein, the *likely* band stays wide until 2225, after which it tightens and remains narrow through 2300.

4 Discussion

4.1 Physical interpretation of future learning of MALI parameters

As described in Sec. 3.1, there is substantial difference in the degree and timing of learning across the six MALI parameters (Fig. 4). The degree of learning is greatest for $\log(\gamma_0)$, with an $\sim$ 10-fold reduction in the across-trajectory *best estimate* of widths of the *very-likely* ranges as more synthetic observations are introduced between 2015 and 2300. The $\log(\gamma_0)$ parameter controls how strongly prescribed changes in ocean thermal forcing translate into changes in ice-shelf basal melting. Because ice-shelf basal melting is the dominant control on grounded ice discharge through its modulation of ice-shelf buttressing, this parameter effectively controls the magnitude of forcing on the glacier system. As anomalies in grounded ice discharge directly contribute to grounded mass change, our synthetic observations of cumulative grounded mass change strongly inform this parameter. Notably, learning about $\log(\gamma_0)$ begins around 2050 (Fig. 4e) when the prescribed ocean thermal forcing first

https://doi.org/10.5194/egusphere-2026-1585
Preprint. Discussion started: 4 May 2026

begins to increase (Fig. 7a), and rapid learning occurs in the subsequent 25 years, with about half of all learning occurring by 2075 (Fig. 4e). Simulated melt rates are proportional to the product of $\log(\gamma_0)$ and the square of thermal forcing, making it relatively easy for the Bayesian calibration to reduce the uncertainty in the true value of $\log(\gamma_0)$ once thermal forcing begins to change and evolving melt rates modulate ice discharge. Consistent with this interpretation, learning rates of $\log(\gamma_0)$ decrease but remain significant between 2075 and 2200, which is a period of slower continued increase in thermal forcing. Finally, further learning tails off after 2200, when changes in thermal forcing become small. In other words, the rate at which ocean conditions change controls the rate at which the calibration can learn about the parameter relating ocean conditions to ice discharge. This is consistent with a more strongly forced system in principle leading to faster learning (Urban et al., 2014). However, interestingly we do not see a change in learning rate of $\log(\gamma_0)$ when most floating ice is rapidly lost between 2125 and 2150 for most trajectories (Fig. 7b). A possible explanation is that the small amount of floating ice remaining through 2200 (Fig. 7e) is still providing sufficient backstress to affect glacier dynamics.

We note that the learning rate of $\log(\gamma_0)$ at a given analysis year is fairly consistent regardless of what the true value of $\log(\gamma_0)$ is, as indicated by the relatively tight uncertainty bands on the width of the *very-likely* ranges across all trajectories over the entire time period (faint green bands in Fig. 4e). This is consistent with our interpretation that changes in thermal forcing are driving the learning about $\log(\gamma_0)$; the linear relationship between $\log(\gamma_0)$ and ice-shelf melting combined with the direct relationship between ice-shelf melting and the grounded mass change observable yield learning of similar rates whether the true value of $\log(\gamma_0)$ is small or large.

The parameter with the second largest degree of learning is the basal slip exponent, q, which exhibits an ~ 8-fold reduction in uncertainty (Fig. 4b). Learning about q occurs at the fastest rate from 2165–2225, just after most of the ice shelf has been eliminated in most trajectories due to intense ice-shelf basal melting (Fig. 7b). This sudden loss of buttressing imparts a strong change to the glacier stress balance, and the resulting change in ice flow speed needed to accommodate that is strongly controlled by the degree of basal plasticity (Nias et al., 2018; Hillebrand et al., 2022; Brondex et al., 2019). Ice flow speed controls grounded ice discharge, allowing q to be constrained with additional synthetic observations of cumulative grounded mass change during this time period when the glacier is responding to a rapid loss of buttressing. We also note that q introduces a strong nonlinearity in how a change in buttressing affects ice discharge: when q is small, small changes in the stress balance impart disproportionately large changes in ice flow speed. This makes the inferred value of q strongly sensitive to synthetic observations of cumulative grounded mass change and contributes to the large degree of learning. This is consistent with Jantre et al. (2024) finding q to be the parameter contributing the most uncertainty to projected sea-level contribution at 2300. Notably, before rapid learning about q has occurred, there is substantial variation in learning rate across trajectories (wide uncertainty bands in Fig. 4b), suggesting that in the absence of large changes in the stress balance, learning about q depends on the true value of q. This is also expected for a strongly nonlinear parameter: the smaller changes in stress balance during the first century may be sufficient to distinguish very small values of q (highly plastic rheology) from the remaining values, but not to strongly differentiate among those remaining values.

The two parameters introducing spatially-uniform scaling to the basal friction coefficient and ice stiffness (C_μ and C_ϕ, respectively) show more modest learning, with $\sim 56\%$ and $\sim 60\%$ uncertainty reductions, respectively, by 2300 (Fig. 4c,d).

https://doi.org/10.5194/egusphere-2026-1585
Preprint. Discussion started: 4 May 2026

The *best estimates* of learning rates for both parameters are fairly uniform over time, with a modest speedup of learning occurring contemporaneously with the rapid learning of q. These parameters were previously found to have only moderate influence on projected sea-level contribution (Jantre et al., 2024), which may help explain the modest degree of learning achieved. Interestingly, both of these parameters exhibit large variation in learning rate across trajectories, but it is unclear whether this reflects dependence of the rate of learning on the true parameter value or whether learning of these parameters is inherently noisy.

The ice-shelf basal melt rate ($\overline{m}$) shows moderate learning, an $\sim 38\%$ uncertainty reduction, by 2300. This parameter represents historical ice-shelf-averaged melt rate and is used to solve for the bias correction term (δT) in the Jourdain et al. (2020) parameterization given a sampled value of $\log(\gamma_0)$. The relatively modest future learning for $\overline{m}$ possibly reflects two factors: (1) it primarily constrains historical rather than future behavior, while $\log(\gamma_0)$ primarily controls the sensitivity of melting to changes in ocean temperature, and (2) its effects are partially confounded with $\log(\gamma_0)$, which is learned much more rapidly.

The calving yield stress (σ_{max}) shows the weakest learning ($\sim 25\%$ reduction in uncertainty), consistent with our finding in Figs. 2 and 3 that the recalibrated *best estimates* for σ_{max} do not consistently converge to the values used to generate the corresponding synthetic future observation trajectories. This is might be due to two reasons. Under present day conditions, Amery Ice Shelf extends beyond its embayment (Fig. 7c), resulting in the ice near the calving front providing little to no buttressing to the grounded ice (Fürst et al., 2016; Reese et al., 2018; Zhang et al., 2020) and therefore calving has negligible impact on the stress balance of the grounded ice and grounded ice discharge. Because of this, our observable of cumulative grounded mass change cannot meaningfully inform the calving parameter when the calving front is in this configuration. In contrast, later in the projections after the extensive ice-shelf melting that eliminates most of the ice shelf (Fig. 7c), there is very little ice-shelf remaining from which calving can occur. Once the calving process is effectively disabled, it becomes impossible to learn more about the calving parameter, noting that σ_{max} was only defined for floating ice and not applied for calving fronts at grounded ice (Jantre et al., 2024). Notably, the small learning about this parameter that does occur happens primarily in the 2100–2200 time period, which is when the calving front generally exists between these two end states.

4.2 Future learning of sea-level contribution projections

Next we consider learning rates of the future sea-level contribution from the Amery sector at years 2100, 2200, and 2300. End-of-century (2100) SLE projections show limited learning over the course of the century despite incorporating synthetic observations at five additional time points into the parameter calibration (Fig. 6a): the *very-likely* range width contracts by only 30%. In fact, by 2090 the *best estimate* of the *very-likely* range width for 2100 sea-level contribution, 4.17 mm SLE (Fig. 6a), is large relative to the *best estimate* of the 2100 sea-level contribution, which is -0.29 mm SLE (Fig. 8). As seen in Fig. 5a, such a wide *very-likely* range around the posterior predictive mean of the 2100 SLE projections by 2090 would likely include 0 mm SLE, indicating that no sea-level contribution may occur by the end of the century. Furthermore, although the *very-likely* range width decreases, the across-trajectory *likely* band widens over this period, indicating increased uncertainty about the future learning. This is related to the fact that, over this time period, the across-trajectory *likely* band widens for all six parameters (Fig. 4), indicating growing variance among parameter learning trajectories.

https://doi.org/10.5194/egusphere-2026-1585
Preprint. Discussion started: 4 May 2026

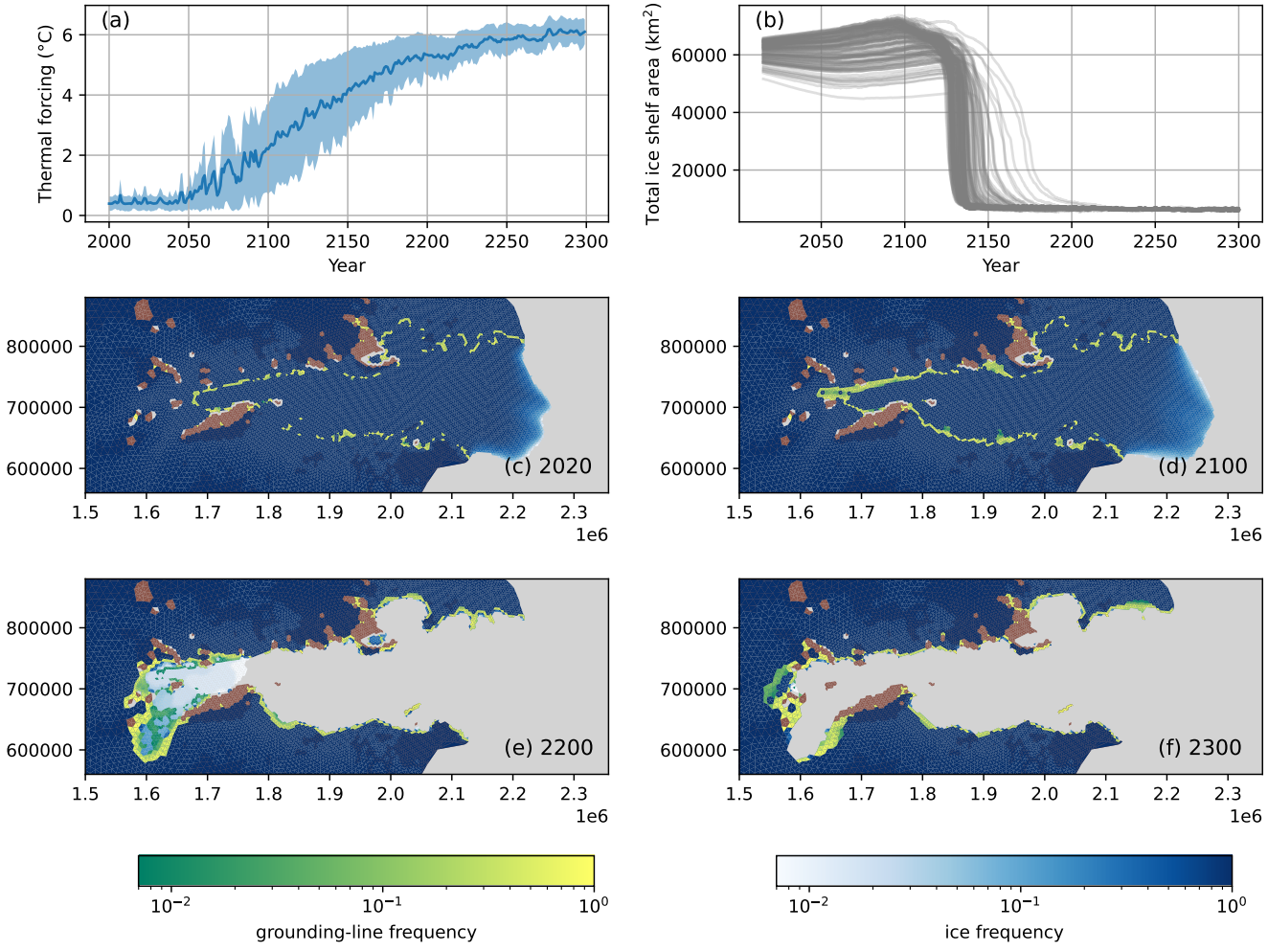

Figure 7. Changes in glacier state affecting future learning. a) Time series of mean thermal forcing ($\pm 1\sigma$) from the UK Earth System Model under SSP5-8.5. This is the same for all trajectories and is the dominant external forcing applied to the glacier system. Modified from Fig. 2 of Jantre et al. (2024). b) Time series of ice-shelf area from all simulations in training set. Despite different parameter values, most simulations experience rapid loss of floating ice around 2150. c-f) Frequency of ice presence and grounding-line position across all simulations. Brown areas represent ice-free land; gray represents open ocean.

4.2.1 Sea-level contribution projections for year 2100

The muted learning of 2100 sea-level contribution from the Amery sector reflects two factors. First, the UKESM SSP5-8.5 forcing that we are applying projects negligible changes to ocean thermal forcing and surface mass balance in this region through 2050 (Jantre et al., 2024), with mean thermal forcing beneath the Amery Ice Shelf remaining below 2°C until approximately 2100 (Fig. 7a). Second, even as thermal forcing increases and ice-shelf thinning begins, the ice sheet's slow geometric response

https://doi.org/10.5194/egusphere-2026-1585
Preprint. Discussion started: 4 May 2026

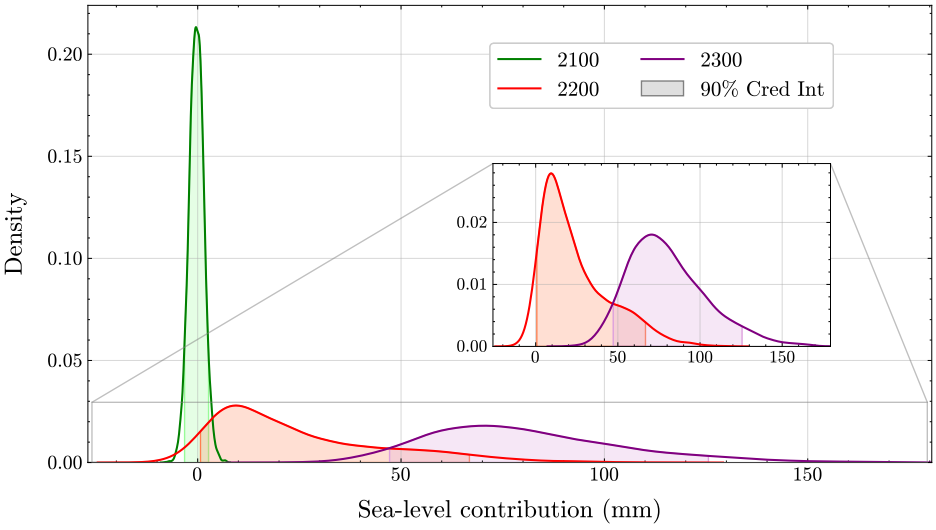

Figure 8. Posterior-predictive distributions for the future sea-level contributions at 2100, 2200, and 2300 derived from the present-day calibration and uncertainty propagation through PCA GP emulator of Jantre et al. (2024).

(Williams et al., 2012) means that parameter perturbations have not yet produced strongly divergent cumulative mass-loss trajectories. This is consistent with the conclusion of Urban et al. (2014) that learning rates are strongly dependent on forcing strength and system response time.

4.2.2 Sea-level contribution projections for year 2200

In stark contrast, the SLE projections for year 2200 exhibit rapid and sustained learning, with an ~ 6-fold reduction in the *very-likely* range width after assimilating observations till 2195 and, paradoxically, an $\sim 70\%$ reduction by 2090 when the *very-likely* range width of the projections for year 2100 had only contracted an $\sim 30\%$ (Fig. 6b). Notably, the distribution of projected sea-level contribution at 2200 based on present-day calibration is wide, spanning a *very-likely* range of 0.69 to 67 mm SLE (Fig. 8), unlike the narrow range of projected sea-level contribution at 2100. By looking at rates of parameter learning (Fig. 4), we observe that the shape of the learning curve for sea-level contribution at 2200 has a similar shape and timing to the learning curve for $\log(\gamma_0)$. We hypothesize that the degree of increase in ice-shelf melting is the dominant control on sea-level contribution at 2200, and because $\log(\gamma_0)$ directly modulates the amount of ice-shelf melting for the prescribed changes in ocean thermal forcing, the ability of the calibration to constrain $\log(\gamma_0)$ is critical for learning about the sea-level contribution at 2200. Once substantial learning about $\log(\gamma_0)$ has occurred through 2075, the majority of learning about the 2200 sea-level contribution is complete.

Interestingly, although the majority of learning about the 2200 sea-level contribution is complete by 2075, there remains substantial disagreement across trajectories about the width of the *very-likely* range, as indicated by the span of the across-trajectory *likely* band (shading in Fig. 6b); the uncertainty in the width of the *very-likely* range of the 2200 sea-level contribution

https://doi.org/10.5194/egusphere-2026-1585
Preprint. Discussion started: 4 May 2026

by 2075 is slightly larger than the across-trajectory mean. We can investigate this by examining the sensitivity of the uncertainty in 2200 sea-level contribution to individual parameters. Specifically, we plot the width of the *very-likely* range for the 2200 SLE projections, with calibration based on observations through 2075, as a function of the MALI parameter values used to generate the 100 synthetic future observation trajectories (Fig. 9). Essentially, we sample all trajectories along the slice of Fig. 6b at 2075 and plot their values against MALI parameter values. We see a strong sensitivity of uncertainty in projected 2200 sea-level contribution to $\log(\gamma_0)$, with larger $\log(\gamma_0)$ values yielding larger uncertainty in the 2200 sea-level contribution projections. Conversely, we see little clear relationship for the other parameters. This indicates that, although the substantial learning about $\log(\gamma_0)$ through 2075 greatly reduces uncertainty in the 2200 sea-level contribution projection by 2075, the remaining uncertainty in the SLE projection is still coming from uncertainty about the true value of $\log(\gamma_0)$. Referring back to the learning rate of $\log(\gamma_0)$, we see that even though the fastest learning of this parameter occurs through 2075, almost half of the learning has still not yet occurred by 2075 (Fig. 4e).

4.2.3 Sea-level contribution projections for year 2300

The projections for year 2300 sea-level contribution also show substantial learning, with the *best estimate* of *very-likely* range width reducing an $\sim$ 6-fold, but the rate of learning is more gradual as observations are added between 2015 and 2300 (Fig. 6c). The shape of the learning curve is similar to that of the parameter q (Fig. 4b), consistent with the finding of Jantre et al. (2024) that q is the parameter to which projections of sea-level contribution at 2300 are most sensitive. We note, however, that the *likely* range of 90% credible interval width for the 2300 sea-level contribution is particularly wide through the 22nd century (Fig. 6c), indicating disagreement between trajectories on the uncertainty in the eventual 2300 sea-level contribution. As we did for the 2200 sea-level contribution, we plot the sensitivity of the uncertainty in 2300 sea-level contribution to individual parameters, but this time only consider calibration through 2150, which is the time when the across-trajectory *likely* band is widest (Fig. 10). We note a relationship between parameter value for q and width of *very-likely* range of 2300 sea-level contribution, with smaller values of q retaining larger uncertainty in the eventual 2300 sea-level contribution. Additionally, $\log(\gamma_0)$ shows a more subtle relationship with *very-likely* range width, with the largest uncertainty in 2300 sea-level contribution for intermediate values of $\log(\gamma_0)$.

These observations lead to the question: Why is uncertainty in sea-level contribution at 2200 most sensitive to $\log(\gamma_0)$ while sea-level contribution at 2300 is most sensitive to q? Our interpretation is that 2200 sea-level contribution is most affected by the timing of ice-shelf removal from elevated ice-shelf basal melting, which occurs for nearly all trajectories between 2125 and 2150 (Fig. 7b). This sudden removal of buttressing increases grounded ice discharge and the amount of subsequent sea-level contribution is strongly affected by how early before 2200 this event occurs. However, over time periods longer than a few decades, the impact of the nonlinearity of the ice-sheet dynamic response to loss of buttressing (controlled by q) has time to accumulate, leading to large uncertainty in the eventual 2300 sea-level contribution until enough observations of the dynamic response to ice-shelf loss can be accumulated to sufficiently constrain q.

This physical interpretation also explains why intermediate values of $\log(\gamma_0)$ cause the most uncertainty in 2300 sea-level contribution when only considering observations through 2150. The year 2150 is in the middle of the time period over which

https://doi.org/10.5194/egusphere-2026-1585
Preprint. Discussion started: 4 May 2026

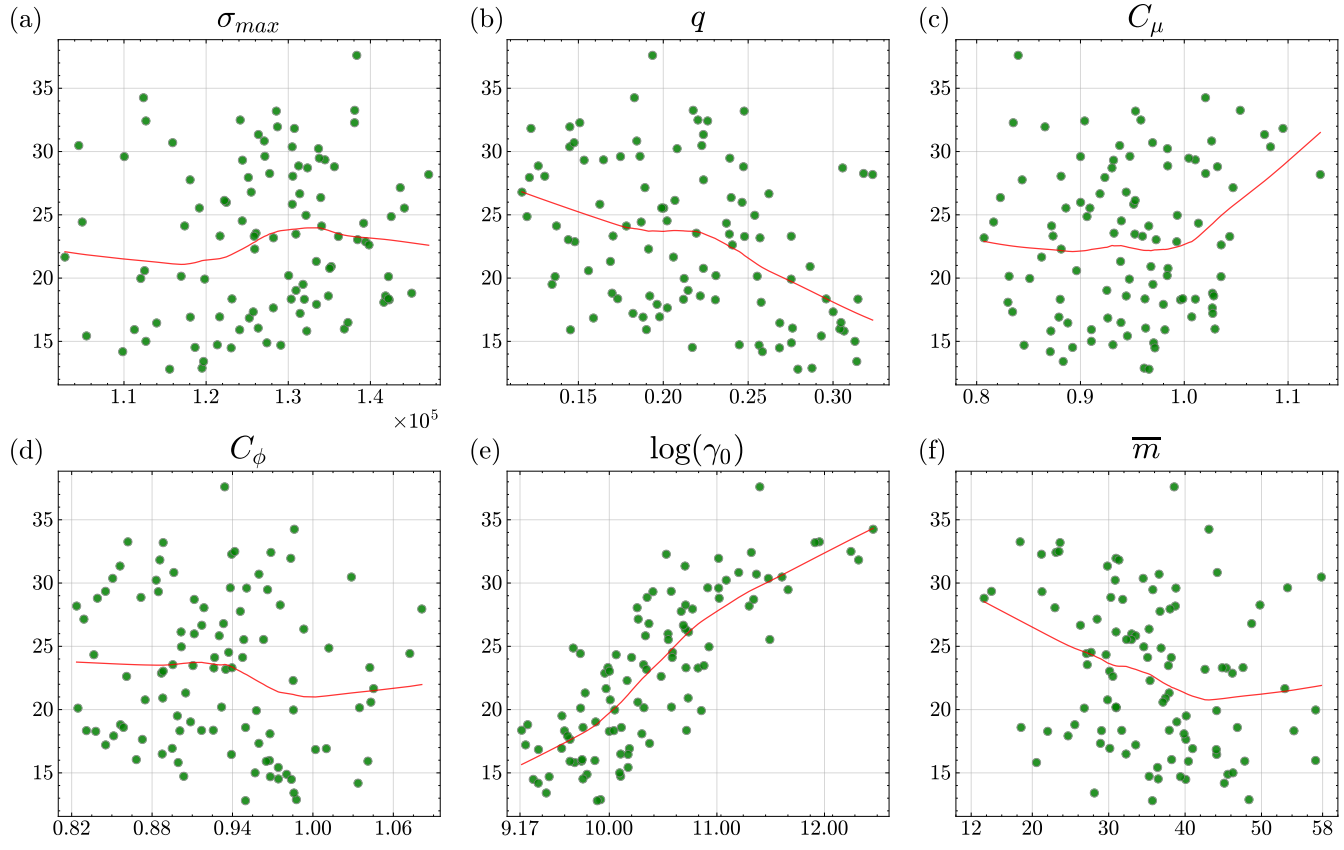

Figure 9. Sensitivity of future learning of year-2200 sea-level contribution to individual MALI parameters informed by observations through 2075**.** Effect of each MALI input parameter on future learning of the year-2200 sea-level contribution (millimeters SLE). For each of the 100 synthetic future-observation trajectories, we perform sequential Bayesian calibration using observations from 2015–2075 and compute the width of the 90% credible interval (*very-likely* range) for the 2200 SLE projections obtained by propagating the recalibrated parameter samples through the PCA GP emulator; smaller widths indicate greater learning. Sensitivity is assessed by relating these across-trajectory *very-likely* ranges to the parameter values used to generate each scenario's synthetic observations. Red curves represent smooth trend line from locally weighted scatterplot smoothing.

ice-shelf removal occurs (Fig. 7b,c). For high values of $\log(\gamma_0)$, which lead to earlier ice-shelf removal, observations through 2150 are already informative of the ice-sheet dynamic response needed to constrain q, leading to lower uncertainty in the eventual 2300 sea-level contribution. For small values of $\log(\gamma_0)$ and associated later ice-shelf removal, the eventual 2300 sea-level contribution will tend to be smaller and absolute uncertainty on smaller sea-level contribution will naturally be smaller than for larger magnitude projections.

https://doi.org/10.5194/egusphere-2026-1585
Preprint. Discussion started: 4 May 2026

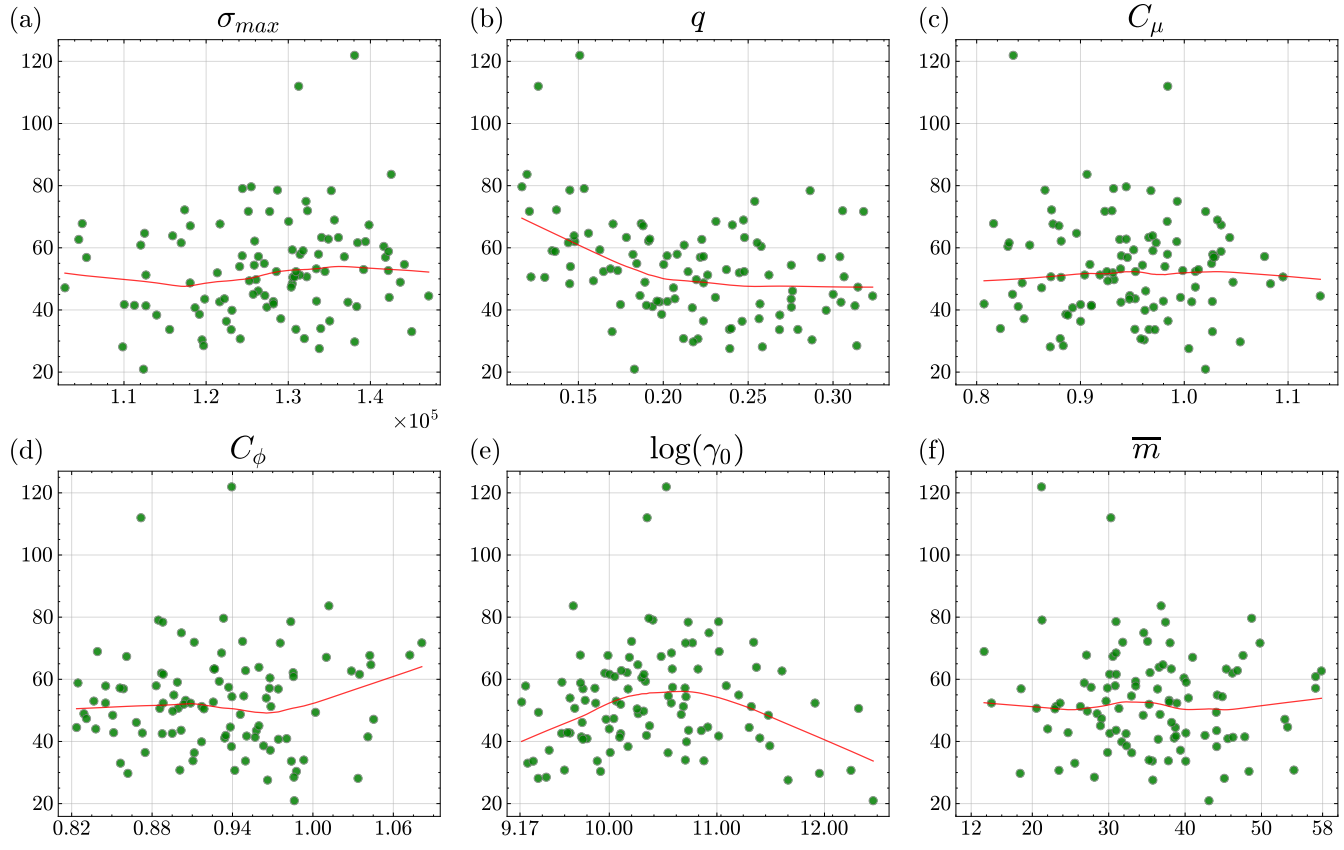

Figure 10. Sensitivity of future learning of year-2300 sea-level contribution to individual MALI parameters informed by observations through 2150**.** Effect of each MALI input parameter on future learning of the year-2300 sea-level contribution (millimeters SLE). For each of the 100 synthetic future-observation trajectories, we perform sequential Bayesian calibration using observations from 2015–2150 and compute the width of the 90% credible interval (*very-likely* range) for the 2300 SLE projections obtained by propagating the recalibrated parameter samples through the PCA GP emulator; smaller widths indicate greater learning. Sensitivity is assessed by relating these across-trajectory *very-likely* ranges to the parameter values used to generate each trajectory's synthetic observations. Red curves represent smooth trend line from locally weighted scatterplot smoothing.

4.2.4 Time-horizon dependence of future learning of sea-level contribution projections

These results bear on the separability of emission scenarios noted by Jantre et al. (2024) and Rosier et al. (2025). Both studies found that SSP1-2.6 and SSP5-8.5 projections remain statistically indistinguishable through much of the 21st century due to large parametric uncertainty, with clear separation emerging only after rapid forcing changes manifest post-2100. Coulon et al. (2025) also found strong overlap between SSP1-2.6 and SSP5-8.5 projections in the 21st century, with uncertainty dominated by choices of model structure, initialization procedure, and parameter values. Beyond 2100, their projections begin to diverge

https://doi.org/10.5194/egusphere-2026-1585
Preprint. Discussion started: 4 May 2026

based on the emissions scenario. Our learning analysis provides a complementary perspective: parametric uncertainty itself contracts substantially only after the ice sheet enters regimes of strong dynamical response.

These sensitivity patterns have important implications for observational strategy and for interpreting learning rates in practice. They suggest that learning will be faster in ice-sheet sectors experiencing strong forcing (large ocean temperature increase and/or high effective melt coefficient) and substantial dynamical response (grounding-line retreat into regions where basal parameters matter). Conversely, stable sectors or those with limited forcing — like the Amery sector prior to 2100 in our simulations — may remain difficult to constrain even with extensive observations. Finally, in addition to needing a strong dynamic response of the system, future learning of a quantity of interest (in this case, sea-level contribution) requires learning about the most important parameters or processes affecting that response (in this case, $\log(\gamma_0)$ and q). Selecting observations that can provide the strongest and earliest constraints on those key processes will be the most valuable. Of note, we have not included observations of velocity, which responds instantaneously to changes in ice-sheet geometry (Williams et al., 2012).

4.3 Comparison with previous learning studies

Previous learning studies have largely focused on climate sensitivity (Urban et al., 2014; Libardoni et al., 2018), air temperatures change (Shiogama et al., 2016), and hydrologic systems and associated infrastructure (Lee et al., 2017; Ceres et al., 2017; Skerker et al., 2023). While future learning of sea-level change has been considered, previous studies have focused on expert judgment, reduced complexity models, and empirical models (Diaz, 2014; Vega-Westhoff et al., 2020), whereas we focus on parameter uncertainty from detailed ice-sheet model simulations of a single sector of the Antarctic Ice Sheet. Direct comparison of the previous learning studies with our study is complicated by fundamental differences in system characteristics. For example, climate sensitivity describes a quasi-equilibrium response to forcing, whereas ice-sheet mass change reflects a transient, path-dependent system with threshold behaviors and long adjustment timescales.

The previous learning studies for these other systems generally share our finding that learning occurs over many decades and stronger forcing leads to faster learning (Urban et al., 2014; Shiogama et al., 2016; Lee et al., 2017; Myhre et al., 2015). An important finding from Urban et al. (2014) was that learning rates were slowest in scenarios of greatest concern (high climate sensitivities) due to longer ocean response times. Our sensitivity analysis (Sec. 4.2) reveals a partially analogous pattern: slower learning (wider *very-likely* ranges) may occur for ice-sheet scenarios with more plastic beds (low q) (Fig. 9b, Fig. 10b), a condition that would lead to larger eventual sea-level contribution. This is also the case for the melt sensitivity to change in ocean temperature in the initial decades when the scenarios yielding the largest sea-level contribution (high $\log(\gamma_0)$) have the least learning (Fig. 9e). However, once multiple decades of ice-sheet response to increased melting creates clear observational signals, this is no longer the case (Fig. 10e).

A notable extension of our methodological framework relative to the work of Urban et al. (2014) on which our methods are based on is explicitly representing uncertainty in the learning rate itself, as considered by Kelly and Kolstad (1999); here we repeat the sequential calibration across 100 synthetic observation trajectories. Urban et al. (2014) acknowledged that conditioning on expected model parameters and sampling only a single projected future for each gives only a noisy point estimate of learning time rather than a distribution of possible learning times. Our approach directly addresses this

https://doi.org/10.5194/egusphere-2026-1585
Preprint. Discussion started: 4 May 2026

limitation, providing *likely* ranges around mean (*best estimate*) learning trajectories that quantify the uncertainty in future learning rates. This uncertainty proves substantial: for $\log(\gamma_0)$, the *likely* range of the 90% credible interval widths at year 2300 spans $[0.136$ to $0.386]$, representing more than 2-fold variation in final uncertainty across different possible future trajectories.

4.4 Limitations and methodological considerations

Our analysis considers only a single scalar observable — cumulative grounded mass change — for post-2015 calibration, whereas the present-day (2015) calibration uses three observables (grounded mass change, grounding-line movement, and calving-front movement). This simplification was adopted for tractability and because cumulative mass change integrates over instantaneous rates, providing a more stable target for emulation. However, it represents a significant limitation, as different observables can provide complementary information about different parameters. Felikson et al. (2023) demonstrated that choice of observable can significantly impact Bayesian calibration outcomes for Greenland Ice Sheet parameters, with spatially resolved observations of surface elevation change, ice velocity, and grounding-line position each constraining different aspects of the parameter space. Our cumulative grounded mass change observable could also obscure important spatial discrepancies between the model and the observations. This would be especially problematic for a larger domain that includes multiple independent outlet glaciers, but in our case it could hide compensating errors between different sub-regions of the domain. Similarly, Libardoni et al. (2018) showed that including spatial patterns of observed surface temperature change impacts learning of climate parameters. We anticipate similar implications of including additional observables in our study on future learning. For instance, including observations of the surface velocity field could increase learning rates, since the velocity field adjusts essentially instantaneously to changes in ice geometry.

The value of different observables might vary by parameter and by forcing regime. For instance, Rosier et al. (2025) found that observations of change in surface ice speed and surface elevation over the period 1996–2021 provided strong constraints on basal friction and ice stiffness parameters for the Amundsen Sea sector. However, they noted that ocean-related parameters were relatively unconstrained by these surface observations alone, suggesting direct observations of ice-shelf thickness change would be a stronger constraint. Similarly, our previous study found that calving front position was the only observation informative of the calving yield stress during present-day calibration (Jantre et al., 2024).

We assume statistical independence among observations across time and across different observables, using diagonal covariance matrices in our likelihood functions. As noted by Jantre et al. (2024), this simplification is adopted due to lack of knowledge about correlation structures. In reality, cumulative grounded mass change observations are serially correlated (since each cumulative value depends on all previous values), and different observables (e.g., mass change, grounding-line position, and ice velocity) are certainly correlated through their shared dependence on ice-sheet state. Proper treatment of these correlations would require specifying space-time covariance structures, a challenging problem that has received limited attention in glaciology but is important for rigorous Bayesian inference (Cressie and Wikle, 2011).

Importantly, we employ a perfect-model assumption: synthetic observations are generated from the same MALI model used for calibration, with discrepancies arising only from emulator approximation error and observational noise. In reality, substantial model structural error exists, arising from unresolved or misrepresented physical processes, inadequate spatial

https://doi.org/10.5194/egusphere-2026-1585
Preprint. Discussion started: 4 May 2026

resolution, and simplified parameterizations. Model structural error can bias parameter estimates and lead to overconfident uncertainty quantification if not properly accounted for (Recinos et al., 2023). For a future learning study in hydrology (Ceres et al., 2017) found that structural uncertainty reduces learning and can even cause negative learning. Finally, our analysis considers only a single GCM (UKESM) and a single emissions scenario (SSP5-8.5) to force the MALI projections used to generate synthetic future observations. Climate model structural uncertainty is large and might exceed parametric uncertainty for many ice-sheet sectors (Seroussi et al., 2023, 2024; Hillebrand et al., 2025; Coulon et al., 2025). Because SSP5-8.5 is a high emissions scenario, the learning we demonstrate using it possibly represents a high end of possible learning, given the evidence we and others see that stronger forcing leads to faster learning.

4.5 Implications for observing systems

The inferred learning rates for both parameters and sea-level contribution projections can be slow, requiring in many cases 50–100 years of observation to substantially reduce uncertainties. Rapid uncertainty reductions may be associated more with the rapid subsurface melt changes present in the mid-22nd century in our scenario leading to stronger forcings on the ice shelf, than they are with the ice sheet itself. This is not surprising, given the timescales of glacier dynamics.

However, this is not to say that greater learning rates are impossible. Our study focused on only a few basin-wide scalar metrics. Additional observation variables, as well as spatially-resolved observations, have the potential to provide stronger constraints. For instance, spatially resolved observations of ice surface elevation change, velocity, and regional mass change have been shown to provide complementary constraints for ice-sheet models (Felikson et al., 2023). However, such an analysis would also require a more careful treatment of spatial and inter-variable covariance (Nias et al., 2019; Felikson et al., 2023), not just in observations but particularly in the model discrepancy (bias or residual error structure) (Kennedy and O'Hagan, 2001; Gramacy, 2020). Additional complications arise from spatial heterogeneity of parameters: to what extent can observations in one basin or region inform the parameter or projections at another (Jiang et al., 2025)?

Our future learning-rate results suggest that the informativeness of observations can vary over time. In our experiments, future learning of model parameters happens most strongly for the ice-shelf melt coefficient ($\log(\gamma_0)$), with faster learning during the mid-21st century; this could be further accelerated by prioritizing sustained measurements that more directly constrain ice-ocean interaction (e.g., ice-shelf thickness change and ocean conditions beneath or near ice shelves) during this period. In contrast, significant learning about glacier basal parameters (e.g., q, C_μ) happens later in our experiments; accelerating learning about those parameters would require new or more data sources.

Our Bayesian learning study can be considered a stepping stone toward optimal observing system design. Uncertainty reduction in parameters and/or projections can be used as a cost function to optimize when considering different observing system characteristics (e.g., locations to prioritize for higher-resolution or higher-frequency sampling). Value-of-information calculations such as ours then become the inner loop within a larger Bayesian optimal experimental design calculation (Rainforth et al., 2024; Roussel et al., 2024).

The learning-rate distributions also enable the calculation of expected value of information (EVI), a decision-theoretic metric quantifying the maximum amount a decision-maker should be willing to pay to obtain perfect information (Raiffa and Schlaifer,

https://doi.org/10.5194/egusphere-2026-1585
Preprint. Discussion started: 4 May 2026

2000). For a given decision problem with specified loss function, EVI is calculated as the expected reduction in loss from making decisions informed by posterior rather than prior distributions of parameters. More broadly, value-of-information analyses in climate economics have shown that the benefits of reducing uncertainty depend on how strongly that uncertainty affects decision-relevant policy choices, particularly in high-damage regions of the uncertainty space (Newbold and Marten, 2014). In addition, learning about tipping points can materially alter optimal policy by updating beliefs about the location of critical transitions over time (Lemoine and Traeger, 2014). In the climate context, Hope (2015) calculated EVI for learning about climate sensitivity under different emissions pathways, finding values ranging from hundreds of billions to trillions of dollars depending on assumptions about adaptation costs and damages. Extending such calculations to the regional ice sheet domain used here is complex due in part to the fact that ice sheet mass change is just one component of sea-level change, and here we are considering only a small fraction of the Antarctic Ice Sheet.

5 Conclusions

This study investigates future learning of uncertain model parameter values and future sea-level contribution for the Amery sector of the Antarctic Ice Sheet. Through sequential Bayesian calibration using synthetic observations drawn from an emulator of future model trajectories, we were able to explore reduction in uncertainty as plausible future information becomes available, as well as how learning itself is affected by differences in possible future trajectories. The degree of learning about parameters varied substantially across different parameters, with learning concentrated in the parameters most related to changes in ocean forcing and the glacier's dynamic response to it. We found limited scope for narrowing projections through the end of the 21st century but rapid learning in the following century after the forcing scenario we used caused loss of the Amery Ice Shelf across all trajectories.

Methodologically, our framework advances ice-sheet uncertainty quantification by applying future learning methods to the ice-sheet domain. The long response time of ice sheets relative to many other components of the Earth system delays substantial learning and highlighted how observations have most value when they capture periods with strong dynamical forcing. We hypothesize that future learning would be more informative for near-term timescales for glacier regions that are currently undergoing rapid change, like Thwaites Glacier, Antarctica, or west Greenland. More generally, our study expands on previous future learning studies of climate systems by the detailed evaluation of the uncertainty in future learning itself and its dependence on parameter values and time horizons. In some cases, uncertainty in future learning is a substantial fraction of the *best estimate* learning rate, and this trajectory dependence should be considered in studies of future learning. Key caveats of our work include the perfect-model assumption, simplified likelihood assumptions, and a focus on aggregated observables; as shown in related Amery work (Jantre et al., 2024), the choice and granularity of observables can strongly condition calibration and, by extension, what can be learned when.

Looking ahead, the value-of-information perspective suggests clear priorities for observational systems of marine ice sheets. Observations that most directly inform ice-shelf buttressing and grounding-line motion, such as front position and retreat rates, spatial mass-balance patterns, basal melt, and grounding-line change, should be sustained. Extending the framework to

https://doi.org/10.5194/egusphere-2026-1585
Preprint. Discussion started: 4 May 2026

multi-observable, spatially resolved constraints, to alternative forcing scenarios, and to structural uncertainties (e.g., calving, sub-ice-shelf mixing) will improve inferences. The next step in sophistication would be to embed formal decision metrics (e.g., expected value of sample information for coastal design thresholds) to further connect observing-system design to adaptive planning. However, to move to this level of integration, improved understanding of observational uncertainties and how to represent them in statistical models is critical.

https://doi.org/10.5194/egusphere-2026-1585
Preprint. Discussion started: 4 May 2026

Appendix A: Emulator validation

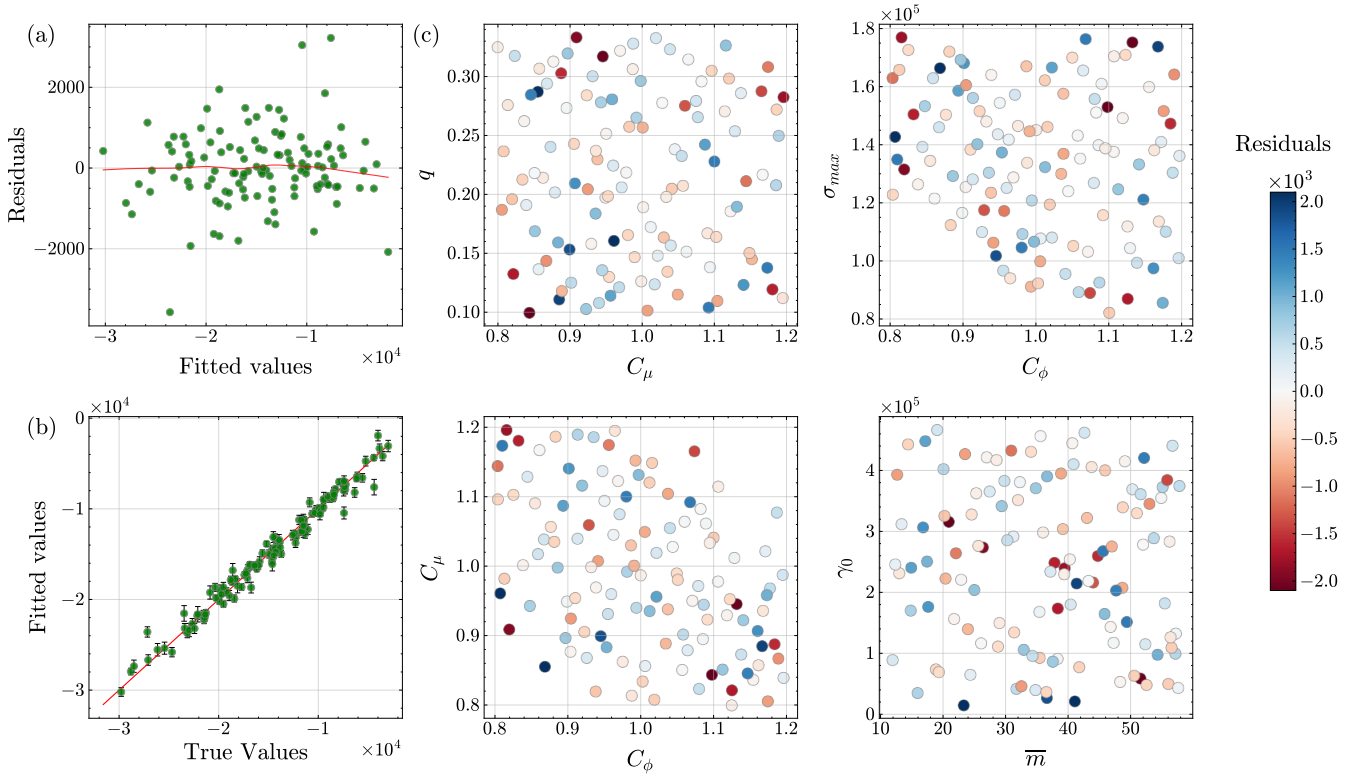

Figure A1. Analysis of Gaussian process emulator fit for cumulative grounded mass change at 2150 obtained from SSP5 projection ensemble: (a) residuals versus fitted values plot, (b) predicted versus actual values plot, and (c) residuals versus pairwise input parameters plots. Colors of residuals are clipped to the colormap range to emphasize overall patterns and reduce outlier influence; values outside the limits are rendered using the colormap range's minimum (for below) or maximum (for above) hue.

The scalar Gaussian-process (GP) emulators for cumulative grounded mass change at each of the 19 analysis years are trained on input-output pairs obtained from the SSP5 projection ensemble. To stabilize emulator training and improve numerical conditioning, we rescale both the MALI input parameters and the scalar output to the unit interval $[0, 1]$, and reverse this transformation when reporting GP predictions. Each year-specific emulator is fit with 5-fold cross-validation. For brevity, we present validation diagnostics only for years 2150 and 2300.

To assess emulator fit, we first plot cross-validated residuals (predicted minus true values) in Figs. A1(a) and A2(a). The residuals are randomly scattered around zero line indicating that the model's assumptions of linearity and constant variance are met. We then compare predicted versus true scalar outputs and overlay central 50% predictive intervals in Figs. A1(b) and A2(b). Points cluster near the 1:1 line and the predictive intervals are narrow, demonstrating strong emulation skill with limited predictive uncertainty. Finally, Figs. A1(c) and A2(c) plot residuals against pairwise input parameters. Herein, we do

https://doi.org/10.5194/egusphere-2026-1585
Preprint. Discussion started: 4 May 2026

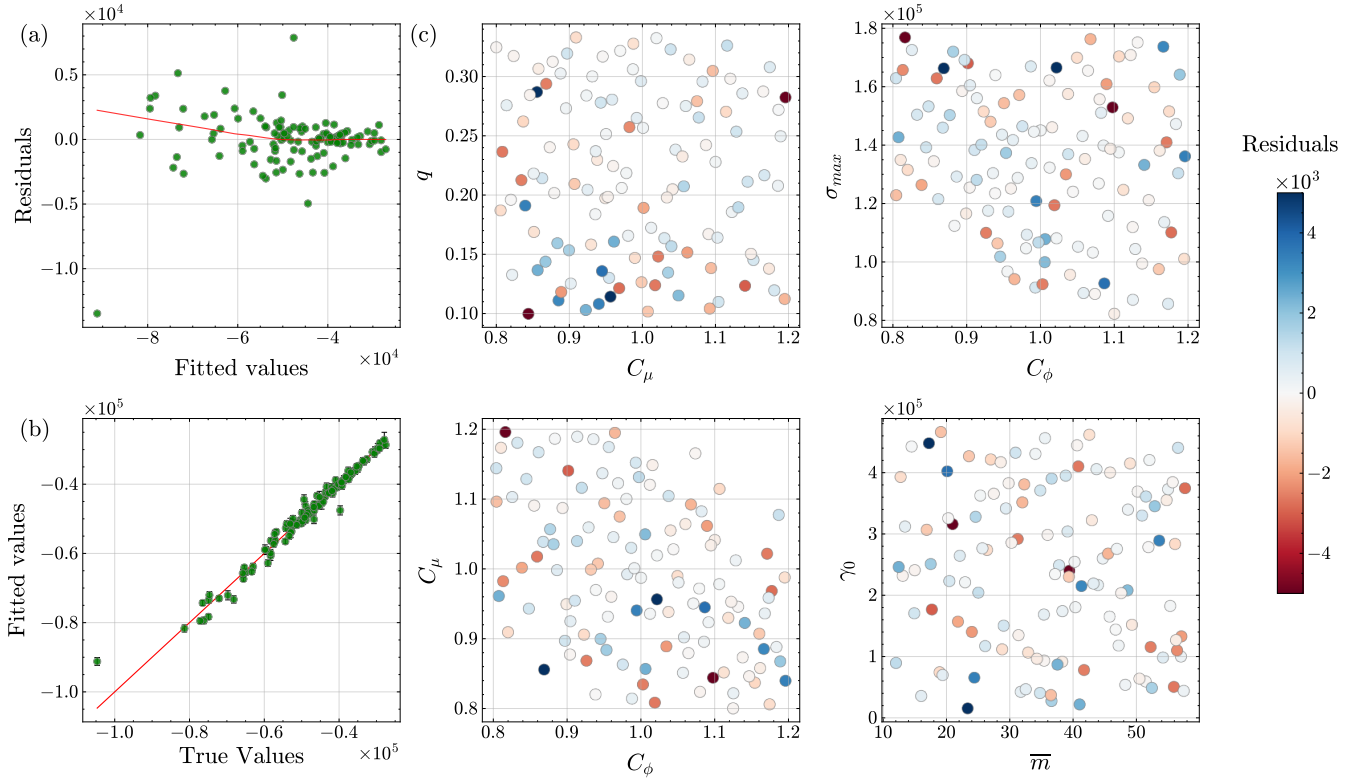

Figure A2. Analysis of Gaussian process emulator fit for cumulative grounded mass change at 2300 obtained from SSP5 projection ensemble: (a) residuals versus fitted values plot, (b) predicted versus actual values plot, and (c) residuals versus pairwise input parameters plots. Colors of residuals are clipped to the colormap range to emphasize overall patterns and reduce outlier influence; values outside the limits are rendered using the colormap range's minimum (for below) or maximum (for above) hue.

not observe meaningful structure or parameter-dependent patterns, suggesting that notable outliers are not driven by particular regions of the input space.

To assess emulation skill jointly across all 19 analysis years, Fig. A3 displays out-of-fold predictions (combined across folds) from the scalar GP emulators (years $2030, 2045, \cdots, 2300$; 15-year spacing) evaluated under 5-fold cross-validation, alongside the corresponding actual (simulated) data from SSP5 projection ensemble. For each realization, year-specific predictions are connected to form a trajectory, which closely follows the simulated path through 2300, indicating consistently strong emulator performance across years. This consolidated view shows that the emulators capture the ensemble's multi-century decline in cumulative grounded mass change while preserving realization-to-realization structure up to 2300.

https://doi.org/10.5194/egusphere-2026-1585
Preprint. Discussion started: 4 May 2026

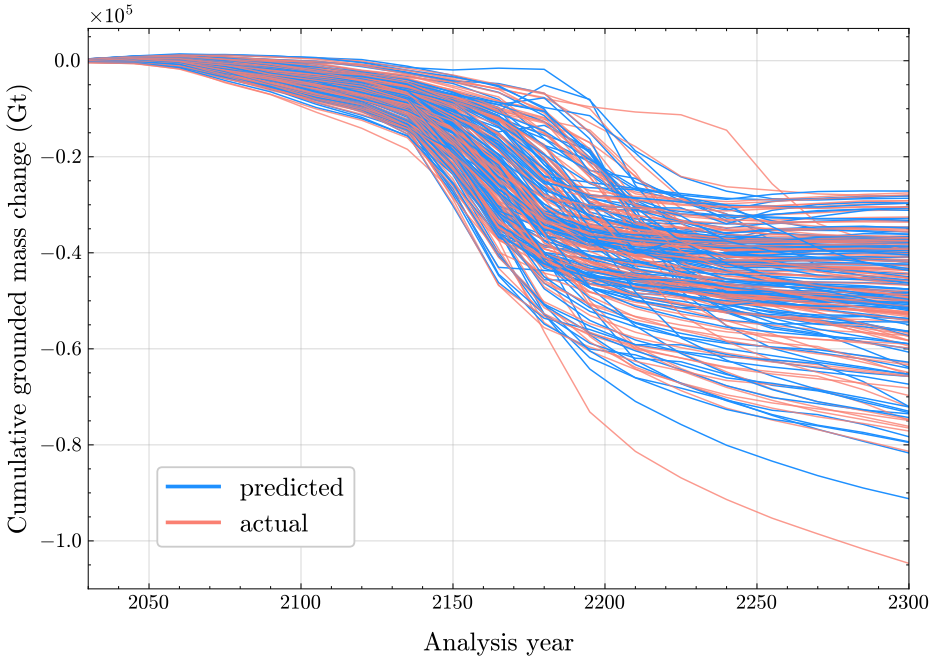

Figure A3. Emulator validation across analysis years. Predictions from 19 scalar Gaussian-process emulators of cumulative grounded mass change for all the analysis years $\{2030, 2045, \cdots, 2300\}$ evaluated under 5-fold cross-validation and compared with "actual" simulated data obtained from SSP5 projection ensemble. For each realization, year-specific predictions are connected with lines to aid visualization of continuity across years, revealing close agreement with the simulation trajectories through 2300 demonstrating strong emulation skill across all emulators.

https://doi.org/10.5194/egusphere-2026-1585
Preprint. Discussion started: 4 May 2026

Appendix B: Future learning analysis continued

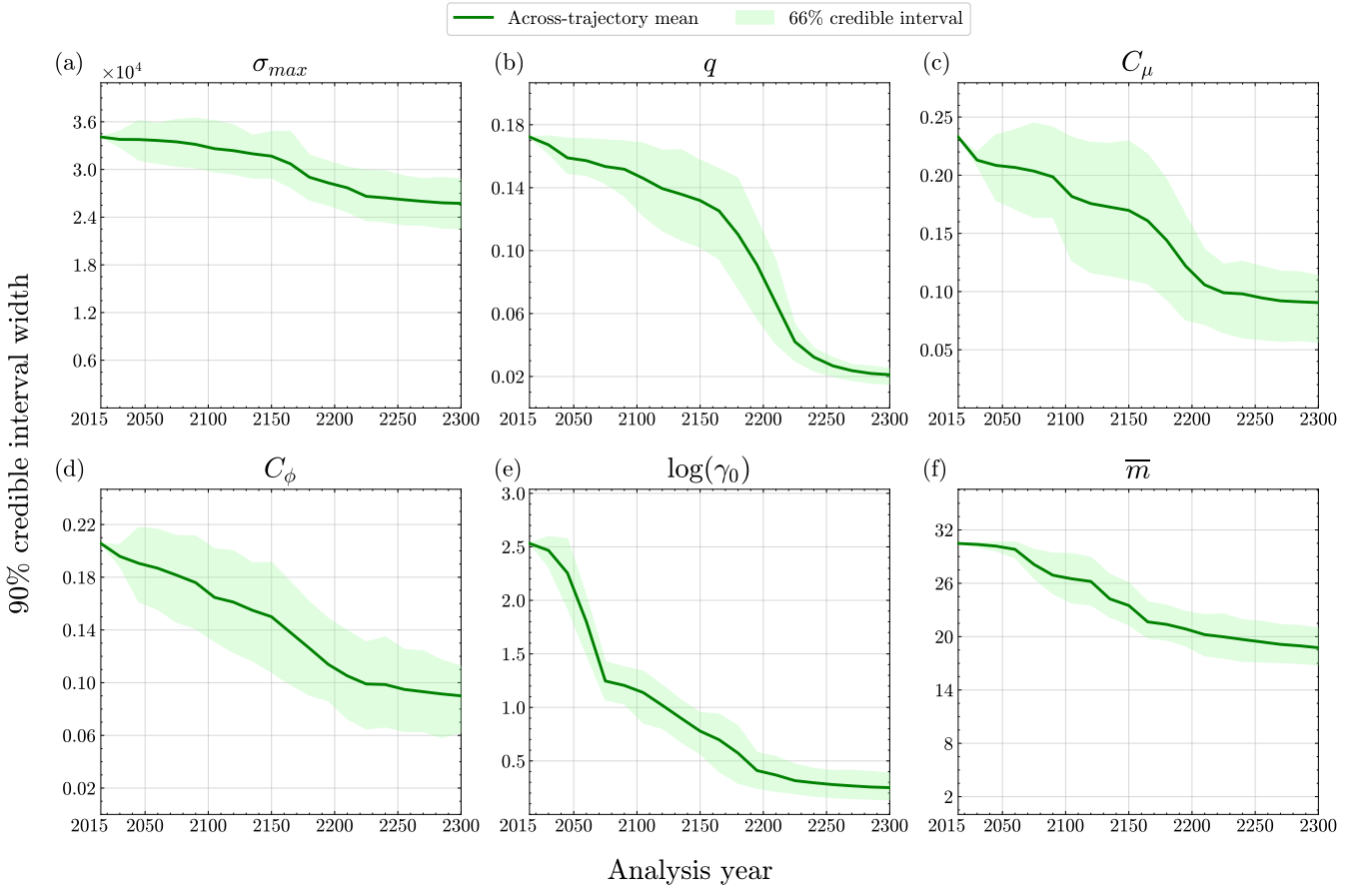

Figure B1. Future learning of MALI parameters. Evolution of parameter uncertainties over time across 100 synthetic future-observation trajectories generated and assimilated using sequential Bayesian calibration. We assess future learning using the width of the 90% credible intervals (*very-likely* ranges) for each parameter at each analysis year across future scenarios; smaller values indicate greater learning. The thick curve is the across-trajectory mean (*best estimate*) trajectory and the shaded band denotes the across-trajectory 66% credible interval (*likely* range), summarizing how quickly uncertainty is expected to contract on average and how uncertain that contraction is, respectively. By 2300, the uncertainties in MALI parameters are reduced substantially for $\log(\gamma_0)$ and q, and moderately for σ_{max}, C_μ, C_ϕ, and $\overline{m}$.

https://doi.org/10.5194/egusphere-2026-1585
Preprint. Discussion started: 4 May 2026

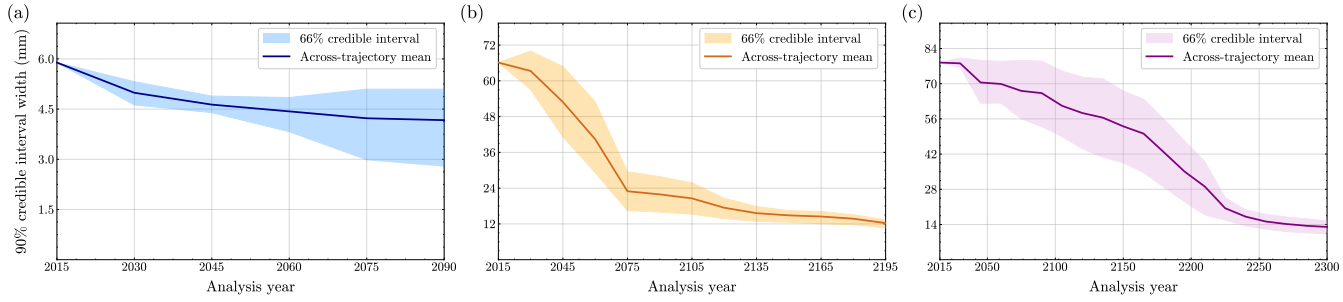

Figure B2. Future learning of sea-level contribution projections. Evolution of sea-level contribution (millimeters SLE) projection uncertainty at (a) 2100, (b) 2200, and (c) 2300 across 100 independent synthetic future-observation trajectories generated and assimilated using sequential Bayesian calibration. We assess future learning using the width of the 90% credible intervals (*very-likely* ranges) for each projection year's sea-level contribution at each analysis year across future scenarios; smaller values indicate greater learning. The thick curve is the across-trajectory mean (*best estimate*) trajectory and the shaded band denotes the across-trajectory 66% credible interval (*likely* range), summarizing how quickly uncertainty is expected to contract on average and how uncertain that contraction is, respectively. Panel (a) typically exhibits muted or gradual declines with increasing uncertainty, reflecting limited end-of-century learning, whereas panels (b) and (c) show more rapid and sustained contraction with decreased uncertainty at longer horizons.

https://doi.org/10.5194/egusphere-2026-1585
Preprint. Discussion started: 4 May 2026

Code and data availability. Code is available on Zenodo at https://doi.org/10.5281/zenodo.17956649. The data and some GP emulator codes are taken from the Zenodo repository https://doi.org/10.5281/zenodo.11166628 associated with Jantre et al. (2024).

Author contributions. ZZ ran all the statistical analyses with input from SJ and NMU. SJ ran final 100 future trajectories and ZZ analyzed them. ZZ, SJ, and MH prepared the manuscript with contributions from all the co-authors.

Competing interests. The authors declare that they have no competing interests.

Disclaimer. This paper describes objective technical results and analysis. Any subjective views or opinions that might be expressed in the paper do not necessarily represent the views of the U.S. Department of Energy or the United States Government.

Acknowledgements. Support for Zach Zerbe was provided by the U.S. Department of Energy, Office of Science, Office of Workforce Development for Teachers and Scientists, under the Science Undergraduate Laboratory Internships Program (SULI) of Summer 2025. Support for Sanket Jantre, Trevor Hillebrand, Matthew J. Hoffman, and Nathan M. Urban was provided through the Scientific Discovery through Advanced Computing (SciDAC) program funded by the U.S. Department of Energy (DOE), Office of Science, Advanced Scientific Computing Research and Biological and Environmental Research Programs. Brookhaven National Laboratory is supported by DOE's Office of Science under Contract No. DE-SC0012704. Los Alamos National Laboratory is operated by Triad National Security, LLC, for the National Nuclear Security Administration of the U.S. Department of Energy under Contract No. 89233218NCA000001.

Financial support. This research has been supported by the Scientific Discovery through Advanced Computing (SciDAC) program, funded by the US Department of Energy (DOE) Office of Science's Advanced Scientific Computing Research (ASCR) and Biological and Environmental Research (BER) programs, as well as the Science Undergraduate Laboratory Internships Program (SULI) of Summer 2025, sponsored and managed by the US DOE Office of Science's Office of Workforce Development for Teachers and Scientists (WDTS) in collaboration with US DOE laboratories/facilities.

https://doi.org/10.5194/egusphere-2026-1585
Preprint. Discussion started: 4 May 2026

References

Aschwanden, A. and Brinkerhoff, D. J.: Calibrated Mass Loss Predictions for the Greenland Ice Sheet, Geophysical Research Letters, 49, e2022GL099 058, https://doi.org/10.1029/2022GL099058, 2022.

Bakker, A. M. R., Louchard, D., and Keller, K.: Sources and Implications of Deep Uncertainties Surrounding Sea-Level Projections, Climatic Change, 140, 339–347, https://doi.org/10.1007/s10584-016-1864-1, 2017-02.

Berdahl, M., Leguy, G., Lipscomb, W. H., and Urban, N. M.: Statistical Emulation of a Perturbed Basal Melt Ensemble of an Ice Sheet Model to Better Quantify Antarctic Sea Level Rise Uncertainties, The Cryosphere, 15, 2683–2699, https://doi.org/10.5194/tc-15-2683-2021, 2021.

Berdahl, M., Leguy, G., Lipscomb, W. H., Urban, N. M., and Hoffman, M. J.: Exploring Ice Sheet Model Sensitivity to Ocean Thermal Forcing and Basal Sliding Using the Community Ice Sheet Model (CISM), The Cryosphere, 17, 1513–1543, https://doi.org/10.5194/tc-17-1513-2023, 2023.

Bevan, S., Cornford, S., Gilbert, L., Otosaka, I., Martin, D., and Surawy-Stepney, T.: Amundsen Sea Embayment Ice-Sheet Mass-Loss Predictions to 2050 Calibrated Using Observations of Velocity and Elevation Change, Journal of Glaciology, pp. 1–11, https://doi.org/10.1017/jog.2023.57, 2023.

Brondex, J., Gillet-Chaulet, F., and Gagliardini, O.: Sensitivity of centennial mass loss projections of the Amundsen basin to the friction law, The Cryosphere, 13, 177–195, 2019.

Bulthuis, K., Arnst, M., Sun, S., and Pattyn, F.: Uncertainty Quantification of the Multi-Centennial Response of the Antarctic Ice Sheet to Climate Change, The Cryosphere, 13, 1349–1380, https://doi.org/10.5194/tc-13-1349-2019, 2019.

Ceres, R. L., Forest, C. E., and Keller, K.: Understanding the Detectability of Potential Changes to the 100-Year Peak Storm Surge, Climatic Change, 145, 221–235, https://doi.org/10.1007/s10584-017-2075-0, 2017.

Coulon, V., Klose, A. K., Kittel, C., Edwards, T., Turner, F., Winkelmann, R., and Pattyn, F.: Disentangling the drivers of future Antarctic ice loss with a historically calibrated ice-sheet model, The Cryosphere, 18, 653–681, https://doi.org/10.5194/tc-18-653-2024, 2024.

Coulon, V., Klose, A. K., Edwards, T., Turner, F., Pattyn, F., and Winkelmann, R.: From short-term uncertainties to long-term certainties in the future evolution of the Antarctic Ice Sheet, Nature Communications, 16, 10 385, https://doi.org/10.1038/s41467-025-66178-w, 2025.

Cressie, N. and Wikle, C. K.: Statistics for spatio-temporal data, John Wiley & Sons, 2011.

Diaz, D. B.: Integrated Assessment of Climate Catastrophes with Endogenous Uncertainty: Does the Risk of Ice Sheet Collapse Justify Precautionary Mitigation?, in: FEEM Note Di Lavoro/Working Paper Series, 2014.

Edwards, T. L., Nowicki, S., Marzeion, B., Hock, R., Goelzer, H., Seroussi, H., Jourdain, N. C., Slater, D. A., Turner, F. E., Smith, C. J., et al.: Projected land ice contributions to twenty-first-century sea level rise, Nature, 593, 74–82, https://doi.org/10.1038/s41586-021-03302-y, 2021.

Felikson, D., Nowicki, S., Nias, I., Csatho, B., Schenk, A., Croteau, M. J., and Loomis, B.: Choice of observation type affects Bayesian calibration of Greenland Ice Sheet model simulations, The Cryosphere, 17, 4661–4673, https://doi.org/10.5194/tc-17-4661-2023, 2023.

Fjelde, T. E., Xu, K., Widmann, D., Tarek, M., Pfiffer, C., Trapp, M., Axen, S. D., Sun, X., Hauru, M., Yong, P., et al.: Turing. jl: a general-purpose probabilistic programming language, ACM Transactions on Probabilistic Machine Learning, 1, https://doi.org/10.1145/3711897, 2025.

Fox-Kemper, B., Hewitt, H., Xiao, C., Agalgeirsdottir, G., Drijfhout, S., Edwards, T., Golledge, N., Hemer, M., Kopp, R., Krinner, G., et al.: Ocean, Cryosphere and Sea Level Change, in: Climate Change 2021: The Physical Science Basis. Contribution of Working Group

https://doi.org/10.5194/egusphere-2026-1585
Preprint. Discussion started: 4 May 2026

I to the Sixth Assessment Report of the Intergovernmental Panel on Climate Change, edited by Masson-Delmotte, V., Zhai, P., Pirani, A., Connors, S., Pean, C., Berger, S., Caud, N., Chen, Y., Goldfarb, L., Gomis, M., et al., pp. 1211–1362, Cambridge University Press, https://doi.org/10.1017/9781009157896.011, 2021.

Fricker, H. A., Young, N. W., Allison, I., and Coleman, R.: Iceberg calving from the Amery Ice Shelf, East Antarctica, Annals of Glaciology, 34, 241–246, https://doi.org/10.3189/172756402781817581, 2002.

Fürst, J. J., Durand, G., Gillet-Chaulet, F., Tavard, L., Rankl, M., Braun, M., and Gagliardini, O.: The safety band of Antarctic ice shelves, Nature Climate Change, 6, 479–482, https://doi.org/10.1038/nclimate2912, 2016.

Goelzer, H., Coulon, V., Pattyn, F., de Boer, B., and van de Wal, R.: Brief communication: On calculating the sea-level contribution in marine ice-sheet models, The Cryosphere, 14, 833–840, https://doi.org/10.5194/tc-14-833-2020, 2020.

Gramacy, R. B.: Surrogates: Gaussian process modeling, design, and optimization for the applied sciences, CRC press, 2020.

Hanna, E., Topál, D., Box, J. E., Buzzard, S., Christie, F. D. W., Hvidberg, C., Morlighem, M., De Santis, L., Silvano, A., Colleoni, F., Sasgen, I., Banwell, A. F., van den Broeke, M. R., DeConto, R., De Rydt, J., Goelzer, H., Gossart, A., Gudmundsson, G. H., Lindbäck, K., Miles, B., Mottram, R., Pattyn, F., Reese, R., Rignot, E., Srivastava, A., Sun, S., Toller, J., Tuckett, P. A., and Ultee, L.: Short- and Long-Term Variability of the Antarctic and Greenland Ice Sheets, Nature Reviews Earth & Environment, 5, 193–210, https://doi.org/10.1038/s43017-023-00509-7, 2024.

Higdon, D., Gattiker, J., Williams, B., and Rightley, M.: Computer model calibration using high-dimensional output, Journal of the American Statistical Association, 103, 570–583, https://doi.org/10.1198/016214507000000888, 2008.

Hillebrand, T. R., Hoffman, M. J., Perego, M., Price, S. F., and Howat, I. M.: The contribution of Humboldt Glacier, northern Greenland, to sea-level rise through 2100 constrained by recent observations of speedup and retreat, The Cryosphere, 16, 4679–4700, https://doi.org/10.5194/tc-16-4679-2022, 2022.

Hillebrand, T. R., Hoffman, M. J., Han, H. K., Perego, M., Hager, A. O., Nolan, A., Asay-Davis, X., Price, S. F., Watkins, J., and Carlson, M.: Evolution of the Antarctic Ice Sheet from 2000–2300 and beyond: Model Sensitivity and Uncertainty Analysis Using MPAS-Albany Land Ice, EGUsphere, pp. 1–51, https://doi.org/10.5194/egusphere-2025-3942, 2025.

Hoffman, M. J., Perego, M., Price, S. F., Lipscomb, W. H., Zhang, T., Jacobsen, D., Tezaur, I., Salinger, A. G., Tuminaro, R., and Bertagna, L.: MPAS-Albany Land Ice (MALI): a variable-resolution ice sheet model for Earth system modeling using Voronoi grids, Geoscientific Model Development, 11, 3747–3780, https://doi.org/10.5194/gmd-11-3747-2018, 2018.

Hope, C.: The $10 trillion value of better information about the transient climate response, Philosophical Transactions of the Royal Society A: Mathematical, Physical and Engineering Sciences, 373, 20140 429, 2015.

Jakeman, J. D., Perego, M., Seidl, D. T., Hartland, T. A., Hillebrand, T. R., Hoffman, M. J., and Price, S. F.: An evaluation of multi-fidelity methods for quantifying uncertainty in projections of ice-sheet mass change, Earth System Dynamics, 16, 513–544, 2025.

Jantre, S., Hoffman, M. J., Urban, N. M., Hillebrand, T., Perego, M., Price, S., and Jakeman, J. D.: Probabilistic projections of the Amery Ice Shelf catchment, Antarctica, under conditions of high ice-shelf basal melt, The Cryosphere, 18, 5207–5238, 2024.

Jiang, Z., Isenberg, N. M., Subba, T., Woo, H.-M., Serbin, S. P., Urban, N. M., and Kuang, C.: A framework for parametric and predictive uncertainty quantification in the E3SM Land Model: Assessing the impact of site and observable heterogeneity, Authorea Preprints, 2025.

Jourdain, N. C., Asay-Davis, X., Hattermann, T., Straneo, F., Seroussi, H., Little, C. M., and Nowicki, S.: A protocol for calculating basal melt rates in the ISMIP6 Antarctic ice sheet projections, The Cryosphere, 14, 3111–3134, https://doi.org/10.5194/tc-14-3111-2020, 2020.

Kause, A., Bruine de Bruin, W., Persson, J., Thorén, H., Olsson, L., Wallin, A., Dessai, S., and Vareman, N.: Confidence levels and likelihood terms in IPCC reports: a survey of experts from different scientific disciplines, Climatic Change, 173, 2, 2022.

https://doi.org/10.5194/egusphere-2026-1585
Preprint. Discussion started: 4 May 2026

Kelly, D. L. and Kolstad, C. D.: Bayesian learning, growth, and pollution, Journal of economic dynamics and control, 23, 491–518, 1999.

Kennedy, M. C. and O'Hagan, A.: Bayesian calibration of computer models, Journal of the Royal Statistical Society: Series B (Statistical Methodology), 63, 425–464, https://doi.org/10.1111/1467-9868.00294, 2001.

King, M., Coleman, R., Freemantle, A.-J., Fricker, H., Hurd, R., Legrésy, B., Padman, L., and Warner, R.: A 4-decade record of elevation change of the Amery Ice Shelf, East Antarctica, Journal of Geophysical Research: Earth Surface, 114, https://doi.org/10.1029/2008JF001094, 2009.

Kopp, R. E., Gilmore, E. A., Little, C. M., Lorenzo-Trueba, J., Ramenzoni, V. C., and Sweet, W. V.: Usable Science for Managing the Risks of Sea-Level Rise, Earth's Future, 7, 1235–1269, https://doi.org/10.1029/2018EF001145, 2019.

Leach, A. J.: The climate change learning curve, Journal of Economic Dynamics and Control, 31, 1728–1752, 2007.

Lee, B. S., Haran, M., and Keller, K.: Multidecadal Scale Detection Time for Potentially Increasing Atlantic Storm Surges in a Warming Climate, Geophysical Research Letters, 44, 10,617–10,623, https://doi.org/10.1002/2017GL074606, 2017.

Lee, B. S., Haran, M., Fuller, R. W., Pollard, D., and Keller, K.: A fast particle-based approach for calibrating a 3-D model of the Antarctic ice sheet, The Annals of Applied Statistics, 14, 605–634, https://doi.org/10.1214/19-aoas1305, 2020.

Lemoine, D. and Traeger, C.: Watch your step: optimal policy in a tipping climate, American Economic Journal: Economic Policy, 6, 137–166, https://doi.org/10.1257/pol.6.1.137, 2014.

Libardoni, A. G., Forest, C. E., Sokolov, A. P., and Monier, E.: Estimates of Climate System Properties Incorporating Recent Climate Change, Advances in Statistical Climatology, Meteorology and Oceanography, 4, 19–36, https://doi.org/10.5194/ascmo-4-19-2018, 2018.

Little, C. M., Urban, N. M., and Oppenheimer, M.: Probabilistic framework for assessing the ice sheet contribution to sea level change, Proceedings of the National Academy of Sciences, 110, 3264–3269, https://doi.org/10.1073/pnas.1214457110, 2013.

Myhre, G., Boucher, O., Bréon, F.-M., Forster, P., and Shindell, D.: Declining Uncertainty in Transient Climate Response as CO2 Forcing Dominates Future Climate Change, Nature Geoscience, 8, 181–185, https://doi.org/10.1038/ngeo2371, 2015.

Newbold, S. C. and Marten, A. L.: The value of information for integrated assessment models of climate change, Journal of Environmental Economics and Management, 68, 111–123, https://doi.org/10.1016/j.jeem.2014.01.002, 2014.

Nias, I. J., Cornford, S. L., and Payne, A. J.: New Mass-Conserving Bedrock Topography for Pine Island Glacier Impacts Simulated Decadal Rates of Mass Loss, Geophysical Research Letters, 45, 3173–3181, https://doi.org/10.1002/2017GL076493, 2018.

Nias, I. J., Cornford, S. L., Edwards, T. L., Gourmelen, N., and Payne, A. J.: Assessing Uncertainty in the Dynamical Ice Response to Ocean Warming in the Amundsen Sea Embayment, West Antarctica, Geophysical Research Letters, 46, 11 253–11 260, https://doi.org/10.1029/2019GL084941, 2019.

Noble, T. L., Rohling, E. J., Aitken, A. R. A., Bostock, H. C., Chase, Z., Gomez, N., Jong, L. M., King, M. A., Mackintosh, A. N., McCormack, F. S., McKay, R. M., Menviel, L., Phipps, S. J., Weber, M. E., Fogwill, C. J., Gayen, B., Golledge, N. R., Gwyther, D. E., Hogg, A. McC., Martos, Y. M., Pena-Molino, B., Roberts, J., van de Flierdt, T., and Williams, T.: The Sensitivity of the Antarctic Ice Sheet to a Changing Climate: Past, Present, and Future, Reviews of Geophysics, 58, e2019RG000 663, https://doi.org/10.1029/2019RG000663, 2020.

Pattyn, F. and Morlighem, M.: The Uncertain Future of the Antarctic Ice Sheet, Science, 367, 1331–1335, https://doi.org/10.1126/science.aaz5487, 2020.

Pittard, M. L., Galton-Fenzi, B. K., Watson, C. S., and Roberts, J. L.: Future Sea Level Change from Antarctica's Lambert-Amery Glacial System, Geophysical Research Letters, 44, 7347–7355, https://doi.org/10.1002/2017GL073486, 2017.

Raiffa, H. and Schlaifer, R.: Applied statistical decision theory, John Wiley & Sons, 2000.

https://doi.org/10.5194/egusphere-2026-1585
Preprint. Discussion started: 4 May 2026

Rainforth, T., Foster, A., Ivanova, D. R., and Bickford Smith, F.: Modern Bayesian experimental design, Statistical Science, 39, 100–114, 2024.

Recinos, B., Goldberg, D., Maddison, J. R., and Todd, J.: A Framework for Time-Dependent Ice Sheet Uncertainty Quantification, Applied to Three West Antarctic Ice Streams, The Cryosphere, 17, 4241–4266, https://doi.org/10.5194/tc-17-4241-2023, 2023.

Reese, R., Gudmundsson, G. H., Levermann, A., and Winkelmann, R.: The Far Reach of Ice-Shelf Thinning in Antarctica, Nature Climate Change, 8, 53–57, https://doi.org/10.1038/s41558-017-0020-x, 2018.

Rosier, S. H. R., Gudmundsson, G. H., Jenkins, A., and Naughten, K. A.: Calibrated sea level contribution from the Amundsen Sea sector, West Antarctica, under RCP8. 5 and Paris 2C scenarios, The Cryosphere, 19, 2527–2557, https://doi.org/10.5194/tc-19-2527-2025, 2025.

Roussel, R., Edelen, A. L., Boltz, T., Kennedy, D., Zhang, Z., Ji, F., Huang, X., Ratner, D., Garcia, A. S., Xu, C., et al.: Bayesian optimization algorithms for accelerator physics, Physical review accelerators and beams, 27, 084 801, 2024.

Seroussi, H., Verjans, V., Nowicki, S., Payne, A. J., Goelzer, H., Lipscomb, W. H., Abe-Ouchi, A., Agosta, C., Albrecht, T., Asay-Davis, X., et al.: Insights into the vulnerability of Antarctic glaciers from the ISMIP6 ice sheet model ensemble and associated uncertainty, The Cryosphere, 17, 5197–5217, https://doi.org/10.5194/tc-17-5197-2023, 2023.

Seroussi, H., Pelle, T., Lipscomb, W. H., Abe-Ouchi, A., Albrecht, T., Alvarez-Solas, J., Asay-Davis, X., Barre, J.-B., Berends, C. J., Bernales, J., et al.: Evolution of the Antarctic Ice Sheet over the next three centuries from an ISMIP6 model ensemble, Earth's Future, 12, e2024EF004 561, https://doi.org/https://doi.org/10.1029/2024EF004561, 2024.

Shiogama, H., Stone, D., Emori, S., Takahashi, K., Mori, S., Maeda, A., Ishizaki, Y., and Allen, M. R.: Predicting Future Uncertainty Constraints on Global Warming Projections, Scientific Reports, 6, 18 903, https://doi.org/10.1038/srep18903, 2016.

Skerker, J. B., Zaniolo, M., Willebrand, K., Lickley, M., and Fletcher, S. M.: Quantifying the Value of Learning for Flexible Water Infrastructure Planning, Water Resources Research, 59, e2022WR034 412, https://doi.org/10.1029/2022WR034412, 2023.

Urban, N. M., Holden, P. B., Edwards, N. R., Sriver, R. L., and Keller, K.: Historical and Future Learning about Climate Sensitivity, Geophysical Research Letters, 41, 2543–2552, https://doi.org/10.1002/2014GL059484, 2014.

Vega-Westhoff, B., Sriver, R. L., Hartin, C., Wong, T. E., and Keller, K.: The Role of Climate Sensitivity in Upper-Tail Sea Level Rise Projections, Geophysical Research Letters, 47, e2019GL085 792, https://doi.org/10.1029/2019GL085792, 2020.

Wernecke, A., Edwards, T. L., Nias, I. J., Holden, P. B., and Edwards, N. R.: Spatial Probabilistic Calibration of a High-Resolution Amundsen Sea Embayment Ice Sheet Model with Satellite Altimeter Data, The Cryosphere, 14, 1459–1474, https://doi.org/10.5194/tc-14-1459-2020, 2020.

Williams, C. R., Hindmarsh, R. C. A., and Arthern, R. J.: Frequency Response of Ice Streams, Proceedings of the Royal Society A: Mathematical, Physical and Engineering Sciences, 468, 3285–3310, https://doi.org/10.1098/rspa.2012.0180, 2012.

Zhang, T., Price, S. F., Hoffman, M. J., Perego, M., and Asay-Davis, X.: Diagnosing the sensitivity of grounding-line flux to changes in sub-ice-shelf melting, The Cryosphere, 14, 3407–3424, https://doi.org/10.5194/tc-14-3407-2020, 2020.